ORNL/TM-2014/440

Optimization and Testing Results of Zr-Bearing Ferritic Steels

Lizhen Tan
Ying Yang
Oak Ridge National Laboratory

Kumar Sridharan
Beata Tyburska-Püschel
University of Wisconsin-Madison

Approved for public release; distribution is unlimited.

September 2014

OAK RIDGE NATIONAL LABORATORY
MANAGED BY UT-BATTELLE FOR THE US DEPARTMENT OF ENERGY

DOCUMENT AVAILABILITY

Reports produced after January 1, 1996, are generally available free via US Department of Energy (DOE) SciTech Connect.

Website http://www.osti.gov/scitech/

Reports produced before January 1, 1996, may be purchased by members of the public from the following source:

National Technical Information Service
5285 Port Royal Road
Springfield, VA 22161
Telephone 703-605-6000 (1-800-553-6847)
TDD 703-487-4639
Fax 703-605-6900
E-mail info@ntis.gov
Website http://www.ntis.gov/help/ordermethods.aspx

Reports are available to DOE employees, DOE contractors, Energy Technology Data Exchange representatives, and International Nuclear Information System representatives from the following source:

Office of Scientific and Technical Information
PO Box 62
Oak Ridge, TN 37831
Telephone 865-576-8401
Fax 865-576-5728
E-mail reports@osti.gov
Website http://www.osti.gov/contact.html

This report was prepared as an account of work sponsored by an agency of the United States Government. Neither the United States Government nor any agency thereof, nor any of their employees, makes any warranty, express or implied, or assumes any legal liability or responsibility for the accuracy, completeness, or usefulness of any information, apparatus, product, or process disclosed, or represents that its use would not infringe privately owned rights. Reference herein to any specific commercial product, process, or service by trade name, trademark, manufacturer, or otherwise, does not necessarily constitute or imply its endorsement, recommendation, or favoring by the United States Government or any agency thereof. The views and opinions of authors expressed herein do not necessarily state or reflect those of the United States Government or any agency thereof.

ORNL/TM-2014/440

Nuclear Energy Enabling Technologies (NEET) FY 2012 Award

OPTIMIZATION AND TESTING RESULTS OF ZR-BEARING FERRITIC STEELS

Lizhen Tan, Ying Yang (Oak Ridge National Laboratory)
Kumar Sridharan, Beata Tyburska-Püschel (University of Wisconsin-Madison)

Date Published: September 2014

Prepared by
OAK RIDGE NATIONAL LABORATORY
Oak Ridge, Tennessee 37831-6283
managed by
UT-BATTELLE, LLC
for the
US DEPARTMENT OF ENERGY
under contract DE-AC05-00OR22725

CONTENTS

Page

LIST OF FIGURES v
LIST OF TABLES vii
ACKNOWLEDGMENTS ix
EXECUTIVE SUMMARY xi
1. BACKGROUND 1
2. COMPUTATIONAL THERMODYNAMICS AIDED ALLOY DESIGN 3
2.1 COMPUTATIONAL THERMODYNAMICS 3
2.2 ALLOY DESIGNS 3
2.2.1 9Cr FM Steels (T-Alloys) 3
2.2.2 Intermetallic-Strengthened Fe-Cr-Zr Alloys (Z-Alloys) 5
2.2.3 High-Cr Ferritic Steels (L-Alloys) 6
3. ALLOY FABRICATION AND MICROSTRUCTURAL CHARACTERIZATION 8
3.1 ALLOY FABRICATION AND THERMOMECHANICAL TREATMENT 8
3.2 MICROSTRUCTURAL CHARACTERIZATION 9
3.2.1 T-Alloys 9
3.2.2 Z-Alloys 10
3.2.3 L-Alloys 11
4. BASIC MECHANICAL PROPERTIES 12
4.1 HARDNESS 12
4.2 TENSILE PROPERTIES 12
4.2.1 T-Alloys 13
4.2.2 Z-Alloys 15
4.2.3 L-Alloys 17
4.3 CREEP RESISTANCE 18
4.4 THERMAL AGING EFFECTS ON MECHANICAL PROPERTIES 18
5. ION-IRRADIATION EXPERIMENTS 19
5.1 EXPERIMENTAL PROCEDURE 19
5.1.1 Proton Irradiation 19
5.1.2 X-Ray Diffraction and Transmission Electron Microscopy 21
5.1.3 Vickers Microhardness 21
5.2 RESULTS 22
5.2.1 L-Alloys 22
5.2.2 T- and Z-Alloys 25
6. SUMMARY 28
REFERENCES 30

LIST OF FIGURES

Figure **Page**

Figure 1. Calculated temperature-dependent mole fraction of phases in a T-alloy as compared to P91. 4
Figure 2. Calculated temperature-dependent mole fraction of phases in Z-alloys (a) Z6, (b) Z7 and (c) Z9. 6
Figure 3. Calculated temperature-dependent mole fraction of phases in L-alloys of LTZ1 and LNTZ. 7
Figure 4. Optical images (OI) and secondary electron images (SEI) of T-alloys. 9
Figure 5. Bright field (BF) TEM images of alloy TTZ1 as compared to P91. 10
Figure 6. Backscattered electron images (BEIs) of Z-alloys. 10
Figure 7. Backscattered electron images (BEIs) of alloy Z9 aged at 650°C for 575 h. 11
Figure 8. Backscattered electron images (BEIs) of alloy LNTZ in the AR and aged (700°C for 7800 h) conditions. 11
Figure 9. Vickers hardness (HV1) of T-, Z-, and L-alloys as compared to P91. 12
Figure 10. Specification of type SS-3 specimen (unit: inch). 13
Figure 11. Typical tensile stress-strain curves of the T-alloys in the AR and TMT conditions. 14
Figure 12. Temperature-dependent yield strength and total elongation of T-alloys in the AR and TMT conditions as compared to P91. 15
Figure 13. Temperature-dependent yield and tensile strength and total elongation of Z-alloys as compared to P91. 16
Figure 14. Temperature-dependent yield strength and total elongation of L-alloys in the AR and TMT conditions as compared to P91. 17
Figure 15. Plots of stress-creep life and strain-creep time showing the creep resistance of T- and Z-alloys at 650°C. 18
Figure 16. Photos of as-received alloy samples (left) and prepared polished 3-mm disks (right). 19
Figure 17. Sample and thermocouple arrangement in the irradiation stage with six samples ready for 2 MeV proton irradiation at 420°C up to ~1 dpa. 20
Figure 18. Damage profile in a model Fe-15Cr alloy irradiated by 2 MeV protons to a level of 1 dpa at 15 μm. Calculation was performed using SRIM-2012.03 assuming th displacement threshold energies to be 40 eV for all elements. 20
Figure 19. L-alloy sample arrangement and appearance before and after 2 MeV proton irradiation at 420°C up to 0.1 dpa. 22
Figure 20. XRD patterns of L-alloy LTZ1 at various damage levels. The possible Ti-rich peaks are marked in magenta. 23
Figure 21. STEM image of L-alloy LTZ1 before proton irradiation: (a) low magnification and (b) high magnification. 23
Figure 22. (a) STEM image and (b) EDS mapping of L-alloy LTZ1 irradiated with protons at 420°C for up to 0.1 dpa. 24
Figure 23. (a) STEM image and (b) EDS line-scan of L-alloy LTZ1 irradiated with protons at 420°C for up to 1 dpa. 24
Figure 24. (a) STEM image and (b) EDS line-scan of L-alloy LT1 irradiated with protons at 420°C for up to 1 dpa. 24
Figure 25. Vickers hardness (25 gf) changes of the irradiated advanced alloys as compared to their non-irradiated condition. 25
Figure 26. XRD patterns of T-alloy T12 at various damages levels. 26
Figure 27. XRD patterns of T-alloys irradiated up to 1 dpa. Main peaks at 2θ of 45°, 65°, and 82° correspond to diffraction from CrFe (PDF04-033-4099). 26

Figure 28. XRD patterns of Z-alloy Z3 at various damages levels. The possible Zr-rich peaks are marked in red. 27
Figure 29. XRD patterns of Z-alloy irradiated up to 1 dpa. Main peaks at 2θ of 45°, 65°, and 82° correspond to diffraction from CrFe (PDF04-033-4099). 27

LIST OF TABLES

Table **Page**

Table 1. Chemical analysis results (wt.%) of O, N and S in the T-, Z-, and L-alloys. 8
Table 2. Processing of the T-, Z-, and L-alloys 9

ACKNOWLEDGMENTS

This research was sponsored by the U.S. Department of Energy (DOE), Office of Nuclear Energy (NE), the Nuclear Energy Enabling Technologies (NEET) FY 2012 Award. This research was supported in part by the Office of Nuclear Energy, Science and Technology and by the Center for Nanophase Materials Sciences (CNMS), which is sponsored by the Scientific User Facilities Division, Office of Basic Energy Sciences, U.S. Department of Energy. We gratefully acknowledge the support provided by Sue Lesica of DOE-NE and Jeremy Busby of Oak Ridge National Laboratory (ORNL).

The authors are grateful to Todd Allen of Idaho National Laboratory and Philip Maziasz of ORNL for helpful comments during initial alloy development, experiments and reporting and Eric Manneschmidt, Tom Geer, David Harper and Greg Cox of ORNL and Ben Maier, Kim Kriewaldt, Lingfeng He and Alexander Zaug of the University of Wisconsin-Madison for their technical support throughout the project.

EXECUTIVE SUMMARY

The mission of the Nuclear Energy Enabling Technologies (NEET) program is to develop cross-cutting technologies for nuclear energy applications. Advanced structural materials with superior performance at elevated temperatures are always desired for nuclear reactors, which can improve reactor economics, safety margins, and design flexibility. They benefit not only new reactors, including advanced light water reactors (LWRs) and fast reactors such as sodium-cooled fast reactor (SFR) that is primarily designed for management of high-level wastes, but also life extension of the existing fleet when component exchange is needed. Developing and utilizing the modern materials science tools (experimental, theoretical, and computational tools) is an important path to more efficient alloy development and process optimization.

Ferritic-martensitic (FM) steels are important structural materials for nuclear reactors due to their advantages over other applicable materials like austenitic stainless steels, notably their resistance to void swelling, low thermal expansion coefficients, and higher thermal conductivity. However, traditional FM steels exhibit a noticeable yield strength reduction at elevated temperatures above ~500°C, which limits their applications in advanced nuclear reactors which target operating temperatures at 650°C or higher. Although oxide-dispersion-strengthened (ODS) ferritic steels have shown excellent high-temperature performance, their extremely high cost, limited size and fabricability of products, as well as the great difficulty with welding and joining, have limited or precluded their commercial applications. Zirconium has shown many benefits to Fe-base alloys such as grain refinement, improved phase stability, and reduced radiation-induced segregation. The ultimate goal of this project is, with the aid of computational modeling tools, to accelerate the development of a new generation of Zr-bearing ferritic alloys to be fabricated using conventional steelmaking practices, which have excellent radiation resistance and enhanced high-temperature creep performance greater than Grade 91.

Using the thermodynamic database that was developed in Year 1 of this project, three series of ferritic alloys have been developed due to the inherent void swelling resistance of ferrite (body-centered cubic) as compared to austenite (face-centered cubic). They are T-alloys (9Cr FM steels), Z-alloys (intermetallic-strengthened Fe-Cr-Zr alloys), and L-alloys (15Cr ferritic steels). Unlike 9Cr FM steels such as T-alloys and P91, the Z- and L-alloys are fully ferritic alloys, without the ferrite-austenite phase transformation during heating and cooling, leading to easier alloy fabrication. Experimental lab heats (~0.45 kg each) were produced by vacuum arc melting and drop casting, followed by different thermomechanical processing for respective alloy series. Chemical analysis indicated that oxygen impurity could not be consistently well controlled in the small lab heats. A larger heat (~12.7 kg) was produced by Carpenter Technology Corporation and achieved a low level of oxygen content, suggesting that oxygen impurity can be well controlled at industrial facilities.

As compared to P91, T-alloys were designed to have increased MX, reduced $M_{23}C_6$, and eliminated Z-phase for better high temperature strength. Significantly finer MX (~5 nm) precipitates with about two orders of magnitude increase in density have been observed in some of the T-alloys. Z-alloys were designed to have fine eutectic structure of ferrite and Fe_2Zr Laves phase. The fraction of the eutectic component has resulted in significant difference in microstructures of the Z-alloys. Additionally, thermal aging favors the formation of a large number of fine Laves phase particles on the order of ~100 nm in the ferritic matrix. L-alloys were designed to have strengthening sources primarily from Fe_2W-type Laves phase, assisted with grain refinement by Zr addition. Thermal aging of a L-alloy at 700°C for 7800 h manifested the formation of a large number of such Laves particles with size ranging from as small as ~90 nm in the ferritic matrix up to a few hundred nanometers at grain boundaries. The formation of such Laves particles did not result in significant changes in hardness. Thermal aging of the T- and Z-alloys at

600 and 700°C, targeting up to 5000 h, is in progress. The aging effect on microstructures and mechanical properties of these alloys will be explored.

Vickers hardness measurements indicate that T-alloys have hardness close to the upper bound of P91 (265 HV) but L-alloys are slightly lower than the lower bound of P91 (196 HV). Z-alloys exhibited a large variation in hardness from the lower bound of P91 to the values significantly higher than the upper bound of P91. Due to the limited size of the developmental lab heats, type SS-3 miniature specimens were used for tensile and creep rupture tests. L-alloys showed the lowest strength, which is lower than or comparable to P91. T-alloys exhibited the highest strength, significantly higher than P91 at the testing temperatures up to 800°C. Depending on specific alloys, Z-alloys displayed strength either inferior or superior to P91 at temperatures less than ~500°C. However, the high temperature (above 500-600°C) strength of the Z-alloys became similar, which is comparable to T-alloys and noticeably greater than P91. The total elongation of the three series of alloys was lower or comparable to P91, most of which are satisfactory considering the significantly smaller testing specimens used in this work (~1.5% of the gauge cross-section area of the regular specimens used for P91). Creep testing of T- and Z-alloys at 600 and 650°C indicated that Z-alloys had creep resistance comparable or superior to T-alloys, both of which have improved creep resistance as compared to P91.

A total of twelve T-, Z-, and L-alloys were irradiated using 2 MeV protons at 420°C up to either ~0.1 dpa or ~1 dpa. Vickers microhardness measurements indicated the largest radiation hardening of the L-alloys (~120%) and the smallest hardening of the T-alloys (~15-40%) after ~1 dpa irradiation. The Z-alloys exhibited a large variation in hardening (~30-90%), suggesting a strong and variable microstructure effects. XRD and STEM/EDS investigations suggested the formation of a large amount of radiation-induced precipitates in the L-alloys and a small amount in the Z-alloys but none in the T-alloys, which is qualitatively consistent with the largest hardening of the L-alloys and the smallest hardening of the T-alloys. Detailed microstructural characterization of the irradiated samples is in progress.

According to the collected results, the L-alloys exhibited low strength, high radiation hardening, and dynamic precipitation of secondary precipitates during thermal aging and irradiation. Additionally, as suggested by the thermodynamic calculations, α'-phase (Cr-rich) is expected to precipitate during long-term aging and is accelerated by irradiation at temperature below ~500°C due to the high Cr content in the L-alloys. Therefore, alloy development of L-alloys will not be continued. Alloy development efforts will be focused on the T- and Z-alloys, which have superior high temperature strength and radiation resistance.

1. BACKGROUND

Nuclear power currently provides a significant fraction of the United States' non-carbon emitting electric power generation. In future years, nuclear power must continue to generate a significant portion of the nation's electricity to meet the growing power demand, clean energy goals, and ensure energy independence. New reactors will be an essential part of the expansion of nuclear power. However, given limits on new builds imposed by economics and industrial capacity, the extended service of the existing nuclear fleet will also be required. Advanced structural materials with superior performance at elevated temperatures are always desired for nuclear reactors because they can improve reactor economics, safety margins, and design flexibility. They benefit not only new reactors including advanced light water reactors (LWRs) and fast reactors such as sodium-cooled fast reactor (SFR) primarily designed for management of high-level wastes, but also life extension of the existing fleet when component exchange is needed.

Ferritic-martensitic (FM) steels are an important category of structural materials because of their outstanding resistance to radiation-induced void swelling (e.g., ~1 vol.% per 100 displacement-per-atom (dpa) in FM steels versus ~1 vol.% per 10 dpa in austenitic stainless steels at temperatures above 300°C [1]), high thermal conductivity, and low thermal expansion coefficients compared to austenitic stainless steels [2]. The body-centered cubic (bcc) structure of ferrite provides the inherent resistance to void swelling compared to face-centered cubic (fcc) structure of austenitic alloys [3]. The formation of martensite followed by the tempering treatment introduces a large amount of lath boundaries and dislocations into the ferrite matrix, leading to refined precipitates and increased strength with decent fracture toughness [4]. However, the dislocations and lath boundaries are not stable at elevated temperatures, resulting in softening due to the impaired pinning effect induced by the instability of precipitates [4,5]. Zirconium (Zr) has shown many benefits to Fe-base alloys, such as introduced ultrafine new phases, improved coarsening resistance of Zr-bearing phases [6], and reduced radiation-induced segregation (RIS) [7,8]. Thus, it is expected that Zr has a beneficial role in improving high-temperature performance. This project is to develop Zr-bearing ferritic alloys aided by computational alloy thermodynamics.

In contrast to traditional experimental trial-error method, computational alloy thermodynamics, a scientific approach to systematically study the relationship between thermodynamic properties and phase stability, provides effective and economic practices for alloy development. The primary microstructures of new alloys can be simulated on a desktop computer within a short period of time, which guide the design of new alloys for experimental verification and performance examination. To facilitate the development of Zr-bearing ferritic steels, a thermodynamic database of Fe-C-Cr-Mo-Nb-Ti-W-Zr had been developed in Year 1 of this project. The computational thermodynamics tool helped design of Zr-bearing ferritic steels in three series: (I) 9Cr FM, (II) intermetallic-strengthened Fe-Cr-Zr alloys, and (III) high-Cr (> 12Cr) ferritic steels.

During the course of alloy development activities in Year 1, it was found that Zr addition greatly reduces the stable temperature regime of austenite and increases the formation temperature of Laves phase, which prevents the martensite formation. Therefore, only a small amount of Zr has been designed in 9Cr FM steels, which have exhibited tensile properties comparable to or moderately improved over Grade 91. A thermomechanical treatment (TMT) was applied to the alloy showing a moderate improvement, which exhibited refined microstructure and increased hardness. Eutectically formed Fe_2Zr intermetallics in Fe-Cr-Zr alloys led to significant improvements in both strength and ductility at elevated temperatures as compared to Grade 91. The Laves phase displayed excellent coarsening resistance during aging at 750°C for 1800 h. The aging led to slight improvements in creep life without noticeable reductions in creep strain. However, the room temperature tensile ductility of the alloys was poor.

Composition adjustment and appropriate TMTs will be developed to favor dispersive Fe_2Zr particles in the matrix for superior strength with adequate ductility. The developed high-Cr ferritic steels have shown controllable tensile properties by TMTs that favor the formation of an increased amount of refined precipitates. Due to the high affinity of Zr to nitrogen and oxygen, it is critical to minimize those impurities during the fabrication of the Zr-bearing alloys to have superior performance.

This report describes the progress of optimization and testing results of Zr-bearing ferritic steels in Year 2 of this project. It is organized as the following: 1) computational thermodynamics aided alloy design, 2) alloy fabrication and microstructural characterization, 3) basic mechanical properties, 4) ion-irradiation experiments, and finally 5) a summary of the findings.

2. COMPUTATIONAL THERMODYNAMICS AIDED ALLOY DESIGN

2.1 COMPUTATIONAL THERMODYNAMICS

Thermodynamic properties of phases in the Fe-C-Cr-Mo-Nb-Ti-W-Zr system were modeled for the development of Zr-bearing ferritic steels. Computational thermodynamics based on the CALPHAD (CALculation of PHAse Diagram) approach [9] is used to develop thermodynamic models of phases in this multicomponent system. The essence of this approach is to develop self-consistent thermodynamic models of phases which cannot only describe thermodynamic properties but also phase equilibria of materials. The most important component of computational thermodynamics is to develop the thermodynamic database that is a compilation of Gibbs Energy functions of phases in a system. For each Gibbs energy function, there are two components, thermodynamic models and model parameters. The most frequently used models are solution, compound energy formalism, and line compound [10]. The model selection is based on the crystal structures, defect types and ordering information of phases. Model parameters are optimized based on experimental data such as phase boundary and thermodynamic property measurements such as activity and enthalpy of formation. Successful thermodynamic modeling requires simultaneously satisfying different properties of phases using one set of Gibbs energy functions. For multicomponent systems where the experimental information is often lacking, the advantage of this approach is that the Gibbs energies of multicomponent phases can be derived from its constituent lower order systems through different geometric rules such as Redlich-Kister expansions [11]. Based on the obtained Gibbs energies, phase property such as fraction (mole, weight and volume), composition, solidus, liquidus at different temperatures and alloy compositions in an unknown system can be calculated by numerically finding the lowest energy minimum of the system. The software used in this work for computational thermodynamic calculation is Pandat [12].

2.2 ALLOY DESIGNS

Using the thermodynamic database and computational tool that were developed in Year 1 of this project, three series of alloys have been explored. A number of alloys have been designed in each alloy series. The detailed compositions of the alloys are not presented here due to potential proprietary concerns. Examples of the alloys in each alloy series can be found in the previous report [13].

2.2.1 9Cr FM Steels (T-Alloys)

This group of alloys is designated as T-series alloys (Fe-9CrWMoVNbTaTiZr). The T-series FM steels have 9 wt.% Cr and are alloyed with W and Mo for solution strengthening, which favors Laves phase, and Nb, Ta, Ti, and Zr for precipitates (primarily MX-type) strengthening. The 9Cr FM steels are considered because they have lower δ-ferrite formation tendency, lower α' formation tendency under irradiation, and lower tendency to increase the ductile-brittle transition temperature (DBTT) under irradiation, as compared to 12Cr FM steels. The properties generated from this series of alloys will be compared to the commercial 9Cr FM steels such as P91 and/or T91.

The calculated temperature-dependent mole fraction of phases in a T-alloy, named as TTZ1, is shown in Figure 1. The calculated phase fraction of a NIMS heat of P91 [14] is plotted in the same scale in Figure 1 for comparison. Similar to P91, a conventional 9Cr FM alloy, the T-alloy is primarily composed of austenite at high temperatures with a decent range of austenite temperature window, at which normalization treatment is usually conducted, e.g., ~1100°C. The alloying of additional ferrite stabilizers in the T-alloy slightly reduced the austenite temperature window as compared to P91. Ferrite primarily exists at intermediate and lower temperatures, at which tempering is usually conducted, e.g., ~750°C. Similar to P91, this series of alloys experiences the ferrite-austenite phase transformation at temperatures

between about 800 and 850°C. Figure 1 shows a fraction of y-axis ranging from 0-0.025 to facilitate the reading of phases with small fractions. Three precipitate phases, designated as MX (primarily carbides), $M_{23}C_6$ and Laves phase, are predicted in the T-alloy. In contrast, an additional phase, designated as Z-phase, is predicted in P91 at low temperatures, which is transformed by consuming up MX (primarily nitrides) at high temperatures. Comparing to P91 in Figure 1, the T-alloy satisfies the following alloy design expectations of this alloy series: 1) increased amount of MX, 2) reduced amount of $M_{23}C_6$, and 3) suppressed the formation of Z-phase.

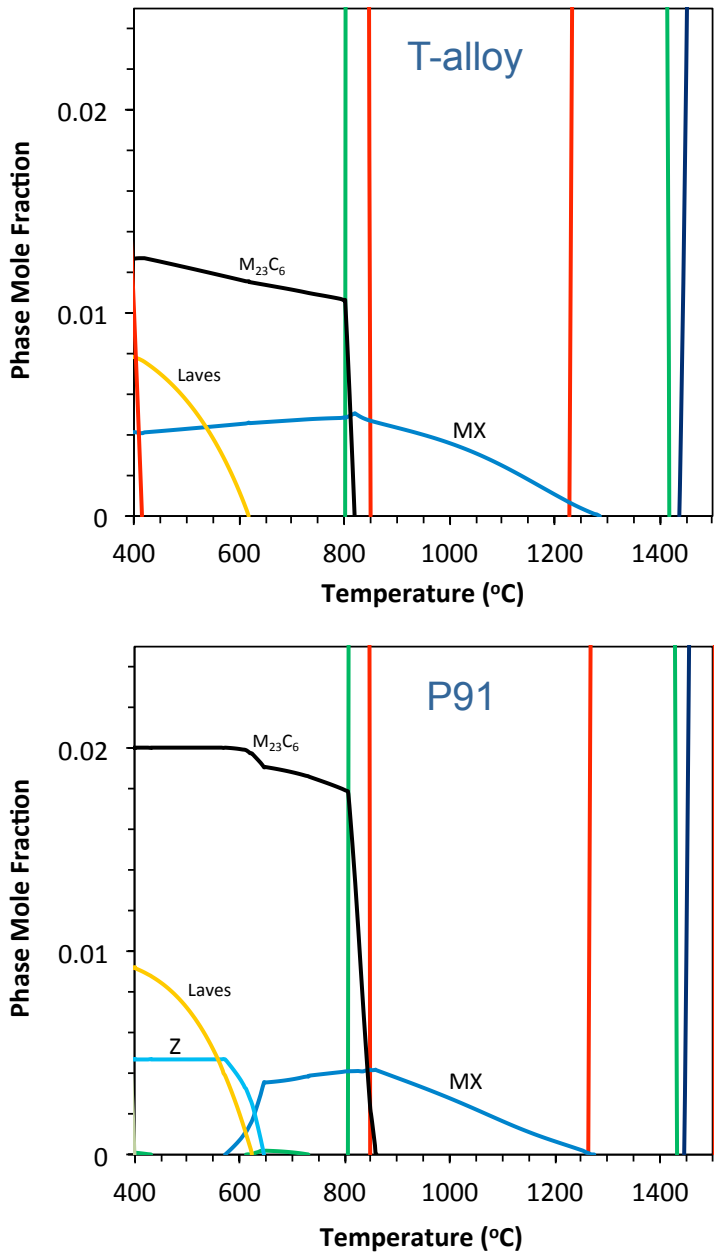

Figure 1. Calculated temperature-dependent mole fraction of phases in a T-alloy as compared to P91.

2.2.2 Intermetallic-Strengthened Fe-Cr-Zr Alloys (Z-Alloys)

This group of alloys is designated as Z-series alloys (Fe-12CrZrWMo). The Z-series alloys are Fe-base ferritic alloys, primarily composed of 12 wt.% Cr and different amounts of Zr with some alloying of W, Mo, Si, Mn, and Ni. The Z-series alloys develop Fe_2Zr-type Laves phase during solidification, leading to fine eutectic microstructures, and form intermetallics following thermomechanical treatment.

Based on the Fe-Cr-Zr ternary phase diagram, the eutectic composition of the Bcc_a2 (ferrite) and Fe_2Zr Laves phases is ~14 wt.% Zr [15]. Z-series alloys are designed to form in-situ composites of Fe_2Zr and Bcc_a2 by forming ultra-fine eutectic microstructure from liquid. The Fe_2Zr intermetallic compound is designed as a strengthening component, and the Bcc_a2 phase provides necessary toughness. The relative amount of each phase is critical to reach a balance of mechanical properties. The Fe_2Zr phase has a hexagonal Laves_C14 structure. It should be noted that there is a substantial amount of Cr participating in the Fe_2Zr_C14 Laves phase. In addition to Cr and Zr, small amounts of Mo, W, Si, Mn, and Ni were also added to tune the properties of materials. The calculated temperature-dependent mole fraction of phases in Z-alloys with alloys Z6, Z7, and Z9 as examples are shown in Figure 2. The Z-alloys are located in the primary phase region of Bcc_a2. Their solidification path is Liquid→Bcc_A2 followed by the eutectic reaction of Liquid→Bcc_A2+Fe_2Zr. The major difference from Z6 to Z9 is the composition of Zr which decreases in sequence, directly leading to the sequential reduction of eutectic in microstructures. In alloy Z6, the polymorphic Laves_C15 (cubic) structure of Fe_2Zr could form, depending on the heat treatment or testing temperature. In alloys Z7 and Z9, only Laves_C14 phase is stable. Compared to T-alloys, Z-alloys do not have a ferrite-austenite phase transformation.

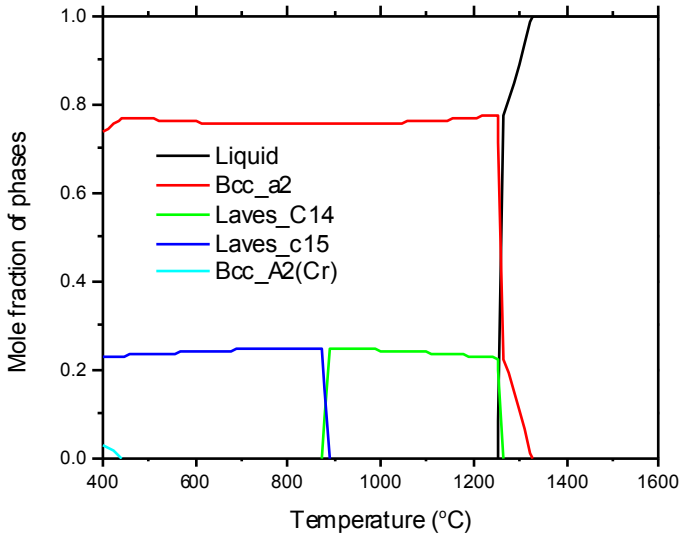

(a)

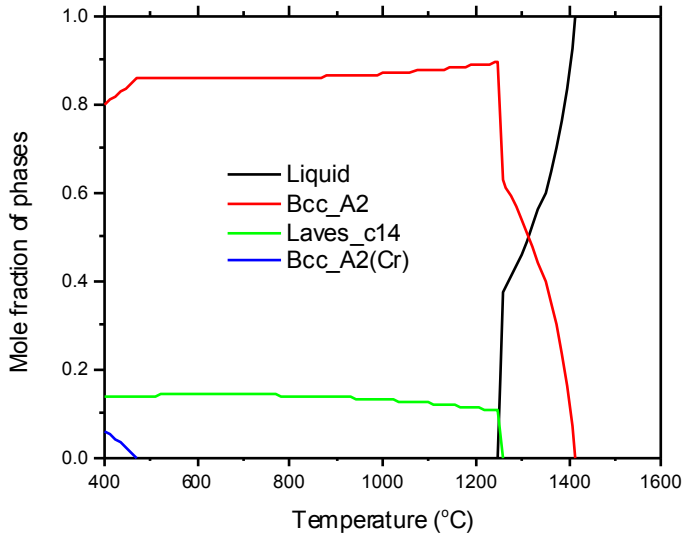

(b)

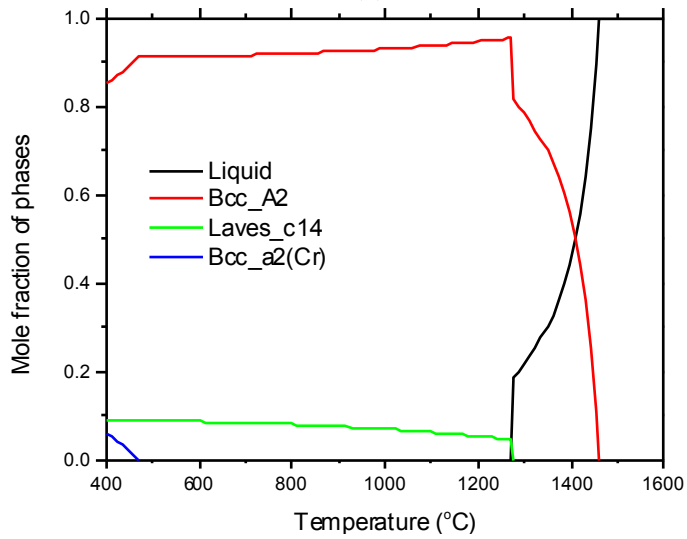

(c)

Figure 2. Calculated temperature-dependent mole fraction of phases in Z-alloys (a) Z6, (b) Z7 and (c) Z9.

2.2.3 High-Cr Ferritic Steels (L-Alloys)

This group of alloys is designated as L-series alloys (Fe-15CrWMoNbTiZr). The L-series alloys are Fe-base ferritic steels, having 15 wt.% Cr and alloyed with W, Mo, Nb, Ti, and Zr. Carbonitrides of Zr, Ti and Nb help grain refinement. Laves phase, primarily Fe_2W-type, precipitates from the ferritic matrix through solid-state reaction during testing and services, which acts as secondary strengthening mechanism in addition to the primary solid solution strengthening. This series of alloys is anticipated to have better corrosion resistance than the lower Cr steels and less stress corrosion cracking (SCC) issues compared to 300-series austenitic stainless steels.

Figure 3 shows the calculated temperature-dependent mole fraction of phases in L-alloys with alloys LTZ1 and LNTZ as examples. Similar to the Z-alloys, L-alloys are fully ferritic matrix below their melting points. The major difference between alloys LTZ1 and LNTZ is the amount of Laves phase and

MX. Alloy LNTZ has an additional σ-phase. As compared to the Z-alloys with 12Cr, the 15 Cr L-alloys favor the formation of α_Cr phase at higher temperatures in greater amounts.

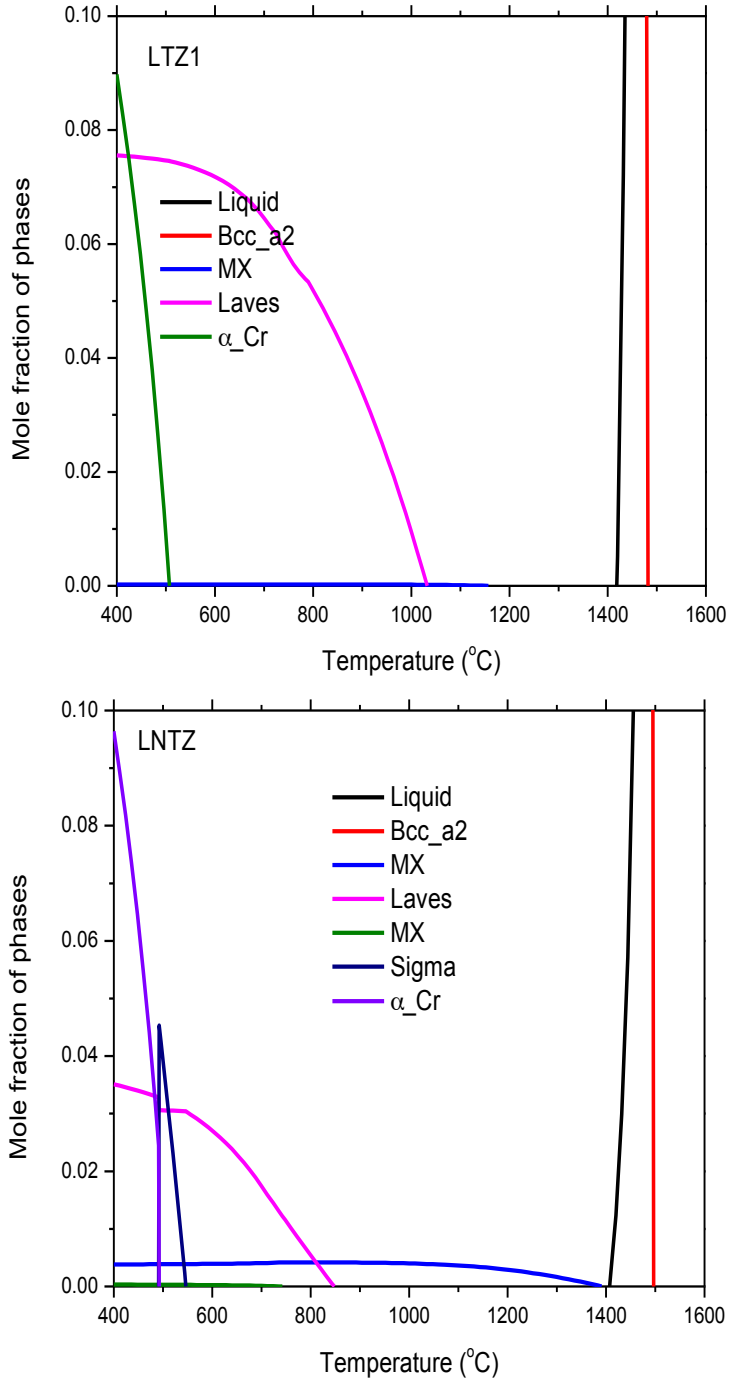

Figure 3. Calculated temperature-dependent mole fraction of phases in L-alloys of LTZ1 and LNTZ.

3. ALLOY FABRICATION AND MICROSTRUCTURAL CHARACTERIZATION

3.1 ALLOY FABRICATION AND THERMOMECHANICAL TREATMENT

Due to the similarity between the T-alloys and P91, the experience on steelmaking and welding of P91 can be directly borrowed for the T-alloys. The lack of ferrite-austenite phase transformation during heating and cooling in the Z- and L-alloys simplifies their steelmaking processes and allows for higher application temperatures as compared to FM steels.

The experimental ingots, about 0.45 kg each with a size of 2.5 × 2.5 × 10.5 cm^3, of the designed alloys have been fabricated using vacuum arc melting and drop casting. Getters of zirconium and titanium were used during the melting and casting to mitigate oxygen and nitrogen contaminations. An example of the chemistry control of the ingots in terms of the amounts of impurities oxygen (O) and sulfur (S) and trace element nitrogen (N) is listed in Table 1. Their contents were analyzed using Instrumental Gas Analysis (IGA). Impurity S was well controlled to an acceptable low level, ranging from 21 to 33 ppm (part-per-million). However, impurity O level was more difficult to control, which ranged from 39 to 460 ppm. The variations in the impurity O level were not closely dependent on the alloyed amount of elements that have high affinity to oxygen. The N level could be relatively well controlled down to <10 ppm by best practice. To examining impurity O level control capability for larger heats, a LNTZ alloy, about 12.7 kg, was fabricated using vacuum induction melting by Carpenter Technology Corporation. The first practice of the LNTZ heat may suggest that impurity O level can be well control at industrial facilities. Furthermore, the application of vacuum arc remelting or electro-slag remelting at industrial facilities will be able to further reduce the impurity content.

Table 1. Chemical analysis results (wt.%) of O, N and S in the T-, Z-, and L-alloys.

Alloy		O	N	S
T-alloys	T1	0.0079	0.047	0.0021
	T2	0.0039	<0.001	0.0024
Z-alloys	Z7	0.023	0.0052	0.0022
	Z8	0.0072	0.0034	0.0027
	Z9	0.0071	0.001	0.0033
L-alloys	LT1	0.046	0.0051	0.0028
	LZ1	0.016	0.035	0.0029
	LTZ1	0.013	<0.001	0.0026
	LNTZ	0.0035	0.0019	0.001

The as-cast ingots of the alloys were subjected to different thermomechanical treatments. The basic processing of the T-, Z-, and L-alloys are listed in Table 2. A homogenization process, which was about 0.8 of the melting temperature of the alloys or as low as the normalization temperature, was conducted on the alloys to obtain homogenous chemical compositions in microvolumes. Hot rolling was applied to the annealed ingots to achieve more than 50% thickness reduction. Cross-rolling was also applied to improve the straightness of the work pieces and reduce textures developed during the rolling processing. Significant amounts of dislocations have been generated during the rolling, which not only increase alloy strength but also serve as nucleation sites of precipitates during the following processing and testing. The Z-and L-alloys were air cooled (AC) after the hot rolling processing. In contrast, the T-alloys were subjected to normalization at about 1100°C after the hot rolling to dissolve as much as possible precipitates in the austenite matrix. The normalized T-alloys were water quenched to ambient temperature and then tempered at 750°C followed by air-cooling. The times for the different types of

heat treatments ranged from 15 to 60 min. depending on the applied temperature and the thickness of the work pieces.

Table 2. Processing of the T-, Z-, and L-alloys

Alloy	Processing
T-alloys	Homogenization + hot rolling + Normalization + Tempering + AC
Z-alloys	Homogenization + hot rolling + AC
L-alloys	Homogenization + hot rolling + AC

3.2 MICROSTRUCTURAL CHARACTERIZATION

Optical microscopy (OM), scanning electron microscopy (SEM), and transmission electron microscopy (TEM) have been primarily employed to characterize the microstructures of the developed alloys.

3.2.1 T-Alloys

The microstructures of T-alloys are presented in Figure 4 using alloys TTZ1 and TT1 as examples. The optical images reveal the overall microstructures at a low magnification, while the secondary electron images exhibit some detailed microstructures at a high magnification. There is no significant difference between the two alloys. Tempered martensite developed in both of the alloys.

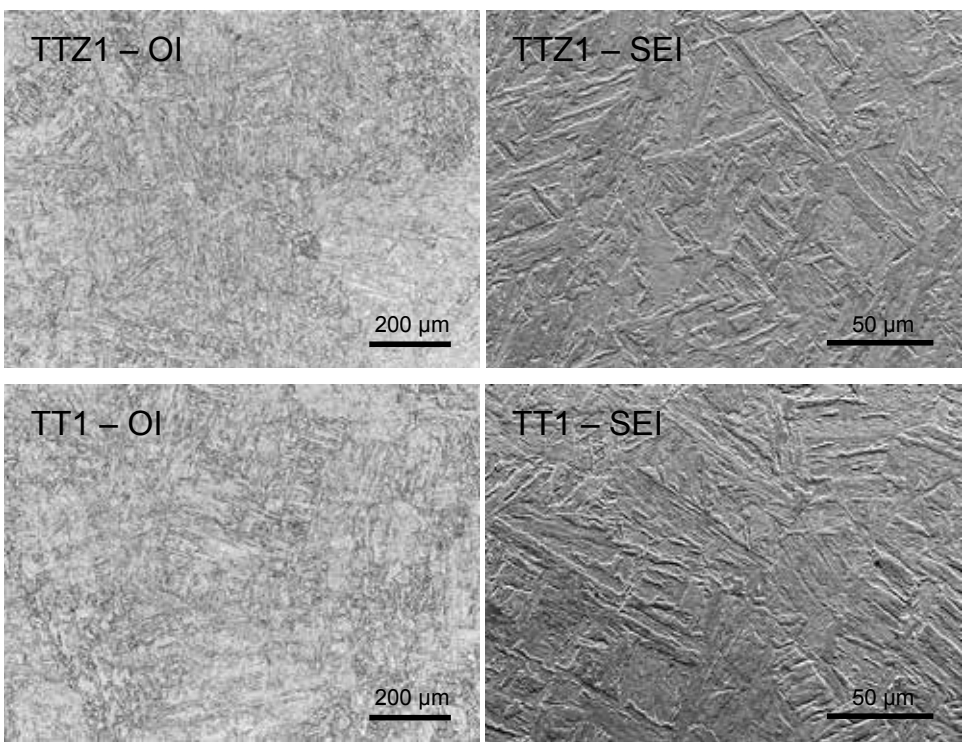

Figure 4. Optical images (OI) and secondary electron images (SEI) of T-alloys.

Bright-field (BF) TEM image of alloy TTZ1, as shown in Figure 5, shows the detailed precipitates and dislocation microstructures. Three $M_{23}C_6$ particles, less than ~100 nm by particle length, precipitated at the prior-austenite grain boundary at the bottom left of the BF image. The lath width is about ~250 nm according to the small contrast variation from the near center to the up right of the BF image. A large amount of ultra-fine precipitates (~5 nm) formed in alloy TTZ1, on the order of 10^{22} m^{-3}. Additionally, a large amount of dislocation on the order of 10^{14} m^{-2} developed in the alloy. The high density of ultrafine precipitates, high density of dislocations, and fine lath width would all contribute to superior strength at high temperatures. For comparison, a BF image of P91 is included in Figure 5, which shows only a few precipitates in nanoscales.

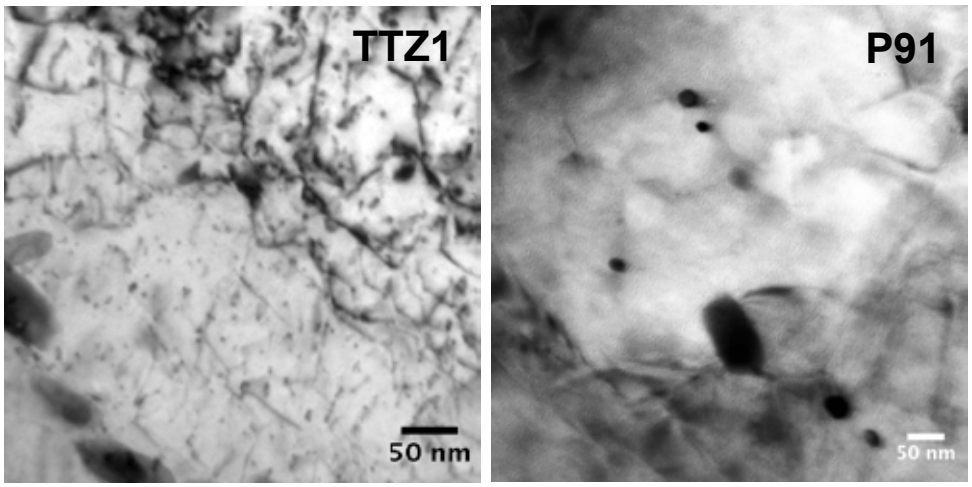

Figure 5. Bright field (BF) TEM images of alloy TTZ1 as compared to P91.

3.2.2 Z-Alloys

Backscattered electron imaging (BEI) mode of SEM was used to examine the microstructures of the Z-alloys. Figure 6 show the examples of alloys Z4, Z7 and Z9 that have a decreasing content of Zr in sequence. The bright white features are eutectic of Fe_2Zr and ferrite, except for the few large white particles in alloy Z4, which are the primary phase of Fe_2Zr. The gray and dark features are ferrite matrix in slightly different grain orientations. Figure 6 indicates the increase of ferrite matrix with the reduction of Zr in the alloys, which is consistent with the calculation results presented in Figure 2.

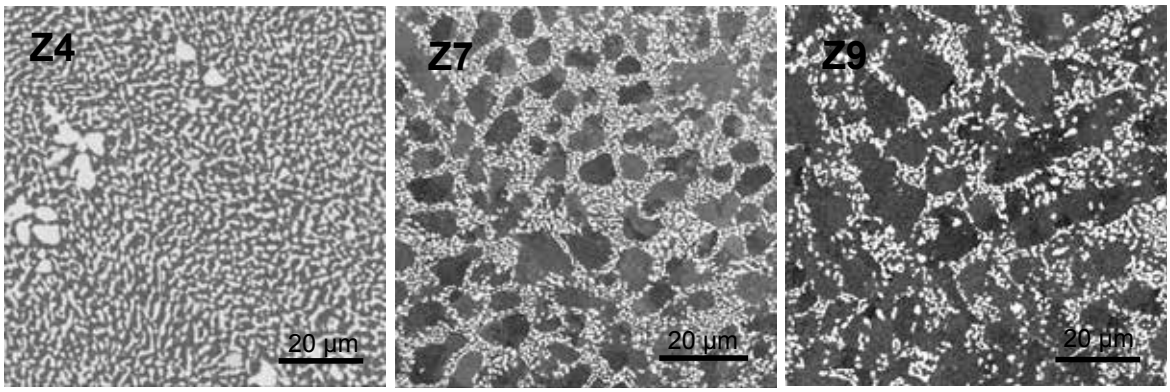

Figure 6. Backscattered electron images (BEIs) of Z-alloys.

Some of the alloys, including the T-, Z-, and L-alloys, are being aged at 600, 650, and 700°C, with a planned time up to 5000 h. Figure 7 shows an example of alloy Z9 aged at 650°C for 575 h. No significantly difference occurred on the eutectic structures according to the BEIs in Figure 6 and 7. However, lots of fine Laves phase particles in a size of ~100 nm formed in the ferrite matrix as shown in the right BEI of Figure 7, which would improve the strength of the alloy after aging.

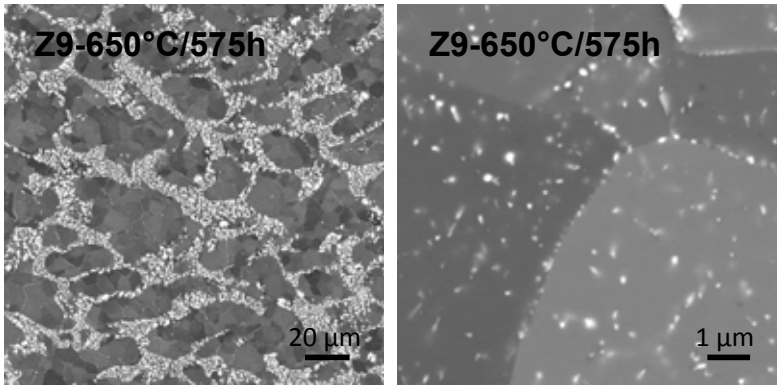

Figure 7. Backscattered electron images (BEIs) of alloy Z9 aged at 650°C for 575 h.

3.2.3 L-Alloys

The microstructure of L-alloys is shown in Figure 8 using alloy LNTZ as an example. The BEI of alloy LNTZ in the as-received (AR) or as-fabricated condition shows many particles in a size of ~2 µm, which refines the microstructure. Thermal aging of the alloy sample was conducted at 700°C for 7800 h. The BEI at a low magnification exhibits many white particles decorating boundaries, which have a size of a few hundred nanometers. A high density of fine white particles in a size of ~90-350 nm is revealed in the ferrite matrix of the BEI at high magnification.

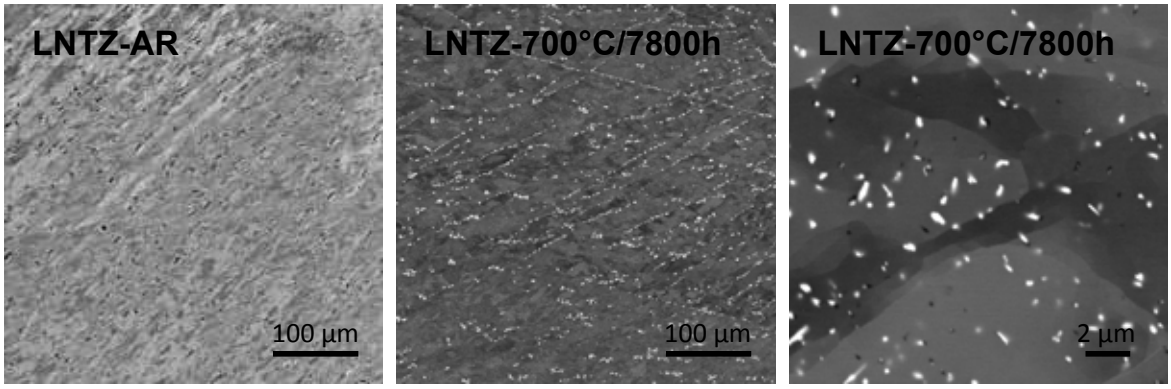

Figure 8. Backscattered electron images (BEIs) of alloy LNTZ in the AR and aged (700°C for 7800 h) conditions.

4. BASIC MECHANICAL PROPERTIES

4.1 HARDNESS

Vickers microhardness measurement was conducted on the metallographic samples according to the ASTM standard E384-11, "Standard test method for Knoop and Vickers hardness of materials." Five measurements with a load of 1 kgf and a holding time of 15 s were conducted for each sample of the designed alloys.

The Vickers microhardness average values of the developed three series of alloys are plotted in Figure 9. Each bar denotes a different alloy. The hardness of T-alloys is in a range of 238-273 HV1, Z-alloys in a range of 207-326 HV1, and L-alloys in a range of 168-203 HV1. As compared to P91, having a hardness range of 196-265 HV specified in the ASTM standard A335-11, "Standard specification for seamless ferritic alloy-steel pipe for high-temperature service", the hardness of T-alloys is about at the higher range of P91. In contrast, the hardness of L-alloys is lower than or comparable to the lower range of P91. Z-alloys exhibited a large variation in hardness from the values similar to the moderate hardness of P91 to that significantly higher than P91.

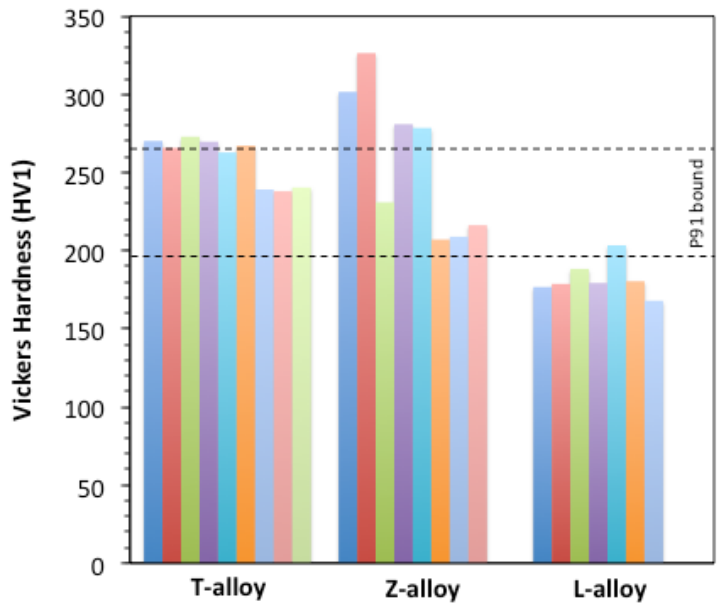

Figure 9. Vickers hardness (HV1) of T-, Z-, and L-alloys as compared to P91.

4.2 TENSILE PROPERTIES

Type SS-3 miniature specimens were used to screen tensile properties of the designed alloys due to their limited heat size. The specification of this type of specimens is shown in Figure 10. The specimens were machined from the heats with specimen length parallel to the longitudinal direction of the heats. Tensile testing was conducted on the specimens at temperatures from ambient temperature up to 800°C in accordance with the ASTM standard E8/E8M-13a, "Standard test methods for tension testing of metallic materials" and E21/E21M-09, "Standard test methods for elevated temperature tension tests of metallic materials." Tests were performed using a MTS tensile testing system with a load cell possessing 22 kN (5,000 lbf) capacity, which is integrated in the load train and placed in the water-cooled zone below the

hot zone of the furnace. Due to the small specimen size, an extensometer was not used during the tests. Tensile testing was performed at a crosshead speed of 0.0076 mm/s (0.018 in/min), corresponding to a nominal strain rate of 0.001 s^{-1}. The tensile testing system, load cells, and furnace thermocouples were regularly calibrated.

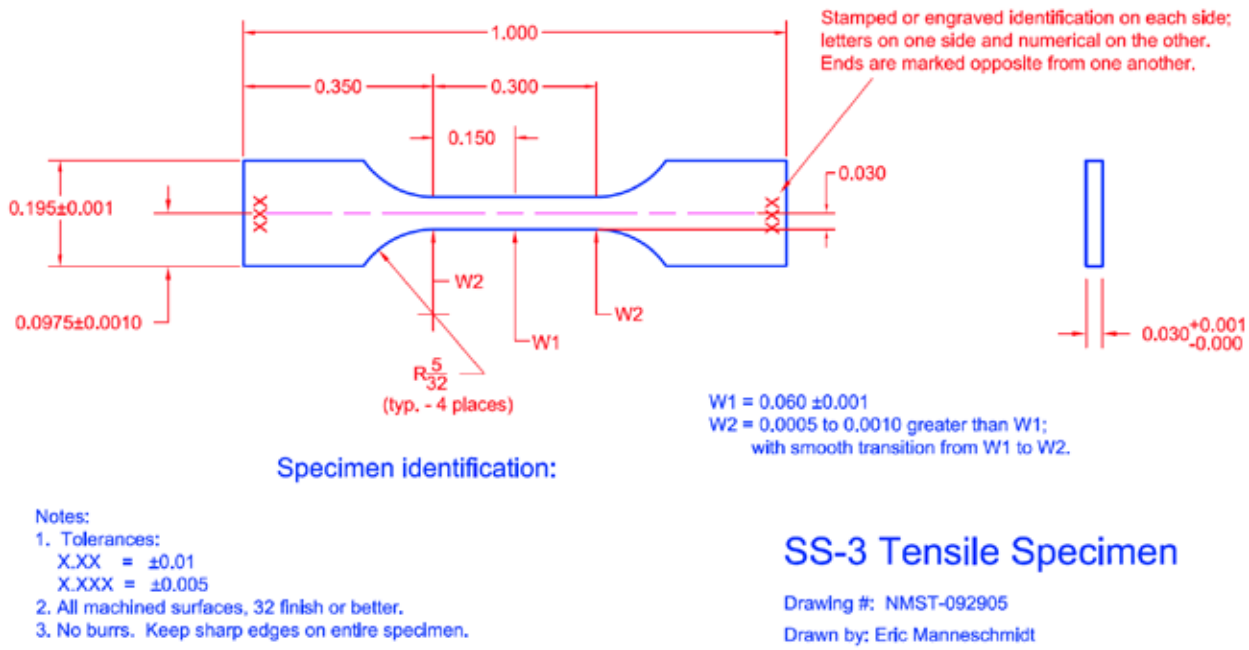

Figure 10. Specification of type SS-3 specimen (unit: inch).

4.2.1 T-Alloys

The tensile stress-strain curves of two T-alloys in the as-received (AR) and a thermomechanical treatment (TMT) conditions are shown in Figure 11. Each line denotes one alloy. Only the testing temperatures of 24, 400 and 700°C are included in this figure. The 400°C test temperature was included because 9-12Cr FM steels usually exhibit the minimum total elongation around this temperature. Figure 11 indicates that the two T-alloys have very similar tensile properties with strength decreasing with the increasing testing temperature and the minimum total elongation at 400°C as compared to the testing at 24 and 700°C. The major difference in Figure 11 is the elongation of the T-alloys in the TMT condition, which is significantly larger than the alloys in the AR condition. The uniform elongations of the TMT samples are noticeably larger than those of the AR samples tested at room temperature.

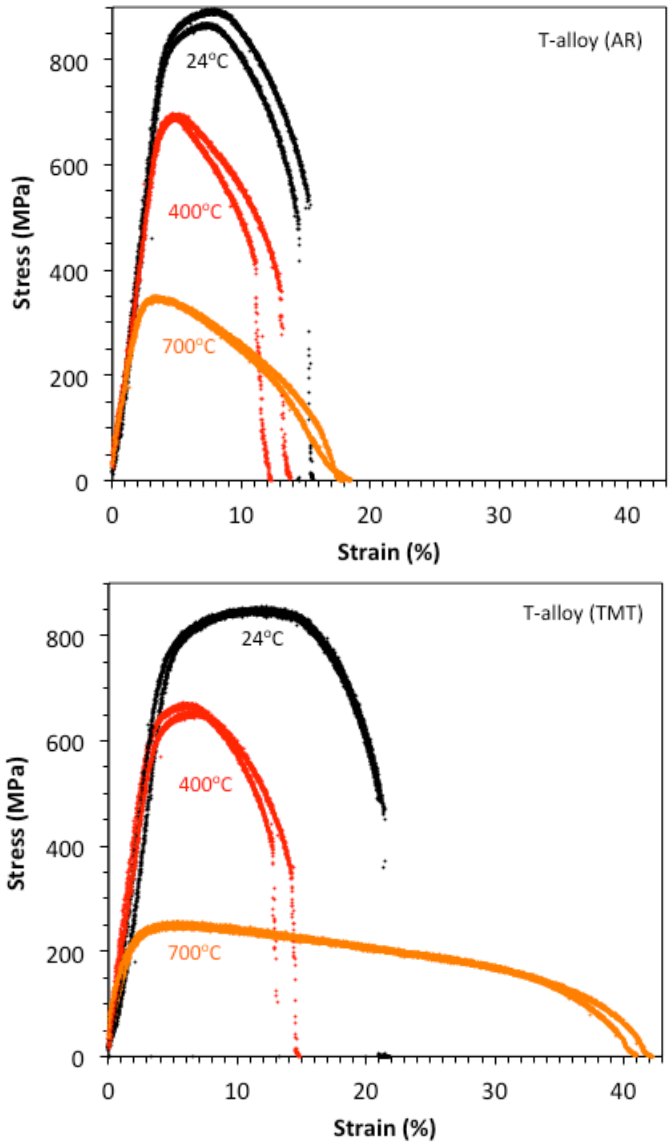

Figure 11. Typical tensile stress-strain curves of the T-alloys in the AR and TMT conditions.

To have a clear picture on the effect of testing temperature on strength and elongation, the testing results of yield strength and total elongation of the two T-alloys are plotted as a function of testing temperature up to 800°C as shown in Figure 12. Each line denotes one alloy. The literature data of P91 are included for comparison [14]. The P91 was tested using regular specimens with a round 10 mm diameter gauge section. The gauge cross-section comparison of the testing specimens used in this work (1.16 mm^2) and the NIMS P91 (78.5 mm^2) is shown as an inset in Figure 12. The two T-alloys have very similar yield strength and total elongation in both the AR and TMT conditions at testing temperatures. The yield strength of the T-alloys in the AR condition is approximately 100 MPa higher than the alloys in the TMT condition. At temperatures above ~550°C, the yield strength of the TMT samples is about 100 MPa higher than P91. Higher strength of alloys is usually associated with lower ductility, which is clearly manifested in the T-alloys in the AR condition having total elongations ranging from ~12% to ~21%. In contrast, the total elongations of the T-alloys in the TMT condition are noticeably greater than the AR condition and close to that of P91, especially considering the significantly smaller specimen size

used in this work. According to the ASTM standard A335-11, a minimum of 20% total elongation is required for P91 tested using regular specimens at room temperature. For miniature specimens, however, the minimum total elongation (E) is calculated by E = 32t (in.) + 10.00, or E = 1.25t (mm) + 10.00. For the SS-3 specimen with a thickness of 0.762 mm (0.03 in.), the minimum total elongation is 10.95% at room temperature. The T-alloys in both the AR and TMT conditions satisfy this requirement. Furthermore, the total elongation of the T-alloys in the TMT condition is expected to be comparable or superior to P91.

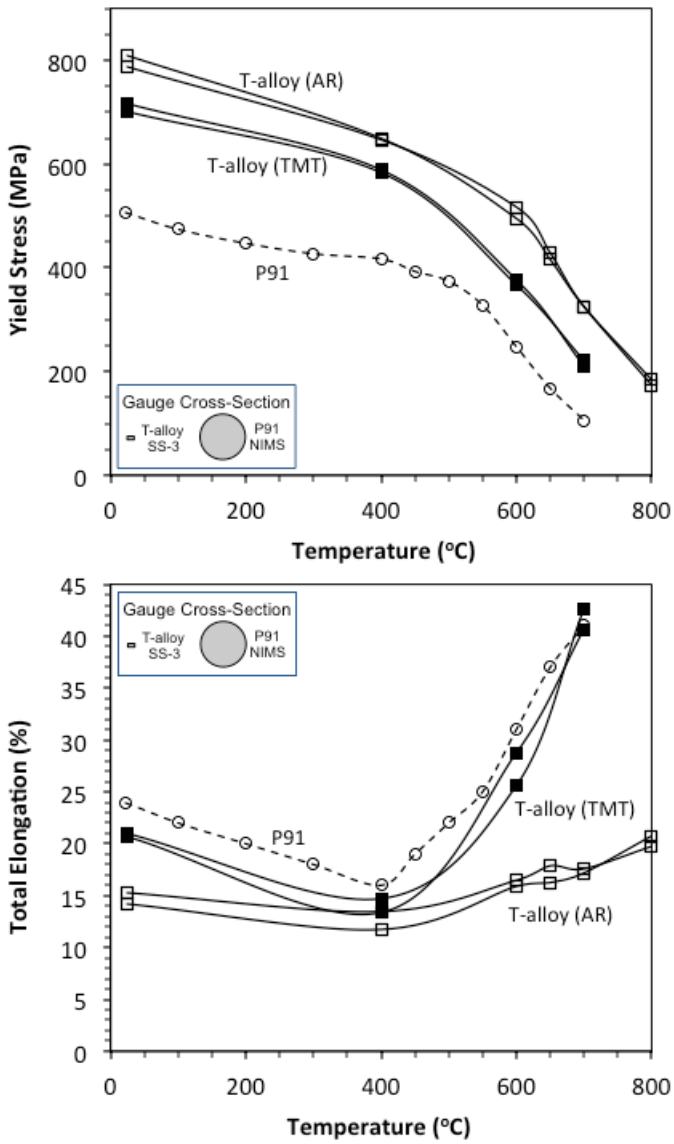

Figure 12. Temperature-dependent yield strength and total elongation of T-alloys in the AR and TMT conditions as compared to P91.

4.2.2 Z-Alloys

Similar to Figure 12, the temperature-dependent yield and tensile strength and total elongation of four Z-alloys are plotted in Figure 13 at testing temperatures up to 800°C. Each line denotes one alloy. The

data of P91 are included for comparison. Yield and tensile strength are denoted using open and solid symbols and lines, respectively.

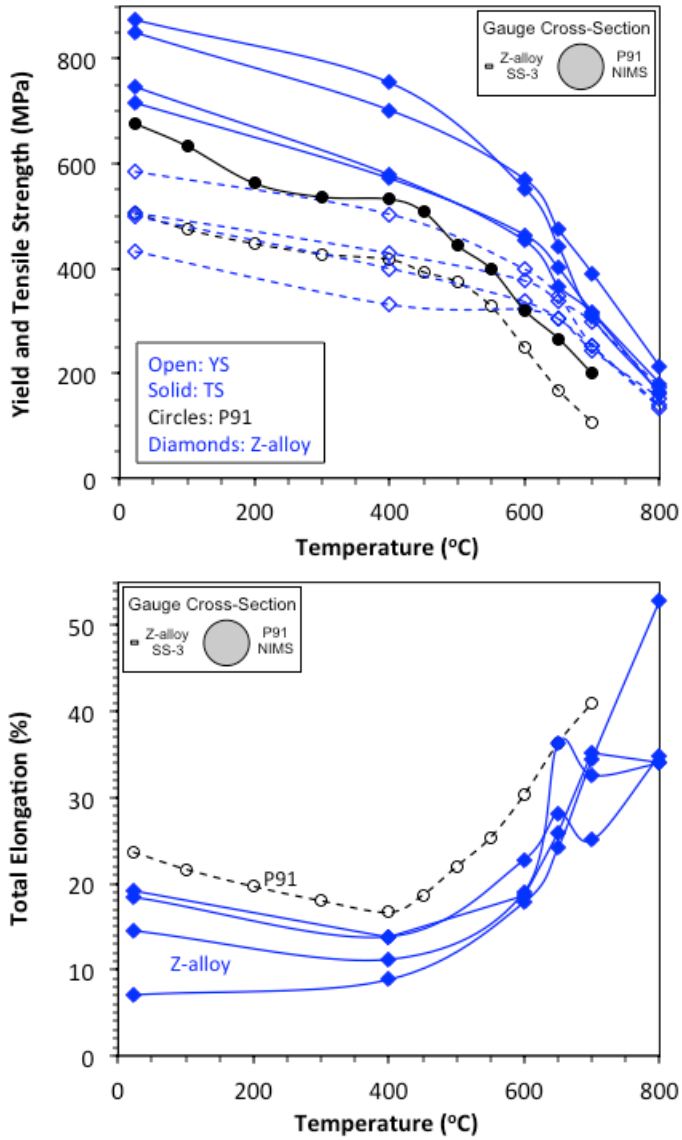

Figure 13. Temperature-dependent yield and tensile strength and total elongation of Z-alloys as compared to P91.

The yield strength of the Z-alloys is lower, comparable, or higher than P91 at temperatures below ~500°C, above which the Z-alloys exhibited greater yield strength than P91. In contrast, the tensile strength of the Z-alloys are greater than P91 at all the testing temperatures up to 800°C. The yield strength of the Z-alloys is lower than that of the T-alloys at temperatures below ~600°C, but then becomes comparable to that of the T-alloys at higher temperatures. The total elongations of the Z-alloys range from ~7% to ~19% at room temperature, which are decent considering the miniature testing specimens. The total elongations approximately increase with increasing temperature up to more than 50% at 800°C, without a distinct minimum total elongation as P91 at 400°C. Figure 13 indicates that Z-

alloys have a large designable range to have a balanced strength and ductility, which have superior strength at high temperatures as compared to P91.

4.2.3 L-Alloys

Similar to Figure 12, temperature-dependent yield strength and total elongation of two L-alloys in the AR and TMT conditions are shown in Figure 14. Each line denotes one alloy in a respective condition. The data of P91 are included for comparison. The L-alloys in the AR condition had lower strength and higher total elongation than P91. The TMT increased the strength of the L-alloys to be comparable to P91 but decreased their total elongation lower than P91. This series of alloys is expected to precipitate secondary Laves phase during thermal aging (e.g., Figure 8) and testing or service, usually under relatively low stresses. Such dynamic precipitation of Laves phase may be accelerated under irradiation condition.

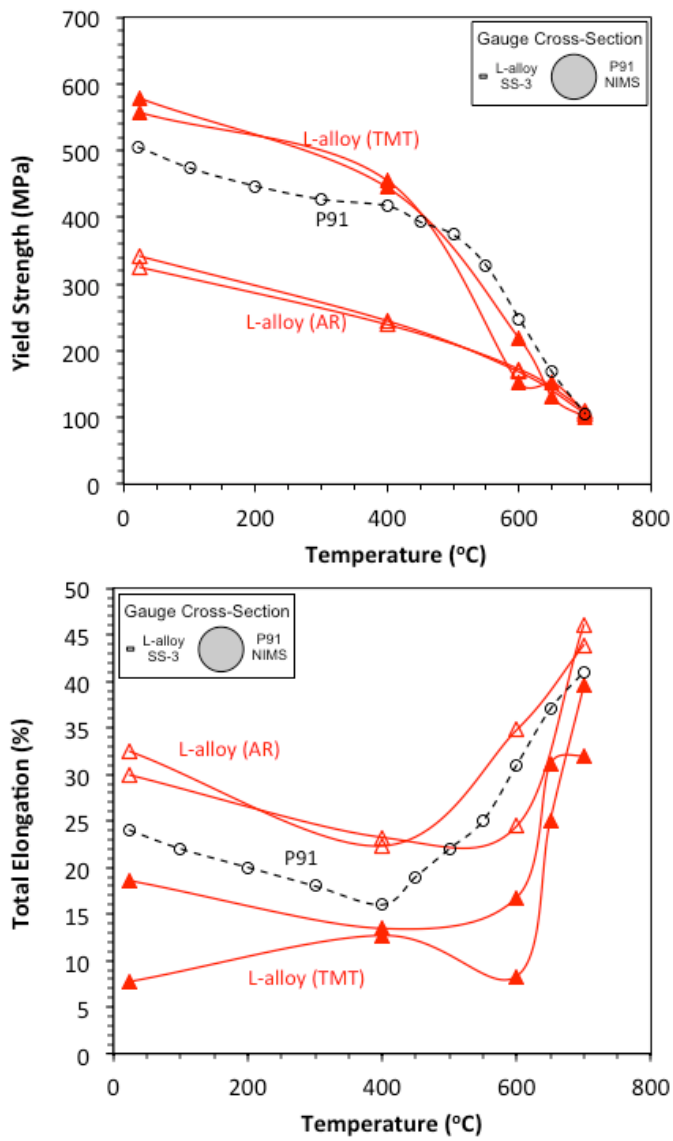

Figure 14. Temperature-dependent yield strength and total elongation of L-alloys in the AR and TMT conditions as compared to P91.

4.3 CREEP RESISTANCE

Type SS-3 miniature specimens, with the specimen length parallel to the longitudinal direction of the heats, were prepared for creep rupture testing. The specimen shoulders were used to apply tensile loads during the tests. The ASTM standard E139-11, "Standard test methods for conducting creep, creep-rupture, and stress-rupture tests of metallic materials," was referenced during the tests. The testing was primarily conducted at 600 and 650°C with a load below 260 MPa. Only a couple of specimens of L-alloys were tested at high loads, which indicated very short creep life, inferior to P91. Therefore, creep testing of L-alloys was not continued. Figure 15 shows an example of the creep resistance of a few T- and Z-alloys in the AR condition at 650°C. The literature data of NIMS P91 [14] and SUS 304-HP stainless steel [16] are included for comparison. The Z-alloys exhibited slightly greater resistance to the creep testing at 650°C as compared to the T-alloys. The limited data indicate that the T- and Z-alloys had creep life comparable or superior to P91, and close to the SUS 304-HP. The creep curves of a T-alloy and a Z-alloy tested at 650°C and 110 MPa in Figure 15 illustrate the creep strain evolutions of the specimens during the creep rupture tests, which had significantly longer creep lives but smaller creep rupture strains than P91. Considering the miniature SS-3 specimen, the creep rupture strains of the T- and Z-alloys are satisfactory. It has been found that Z-alloys had noticeably higher creep rupture strains than T-alloys tested at 600 and 650°C.

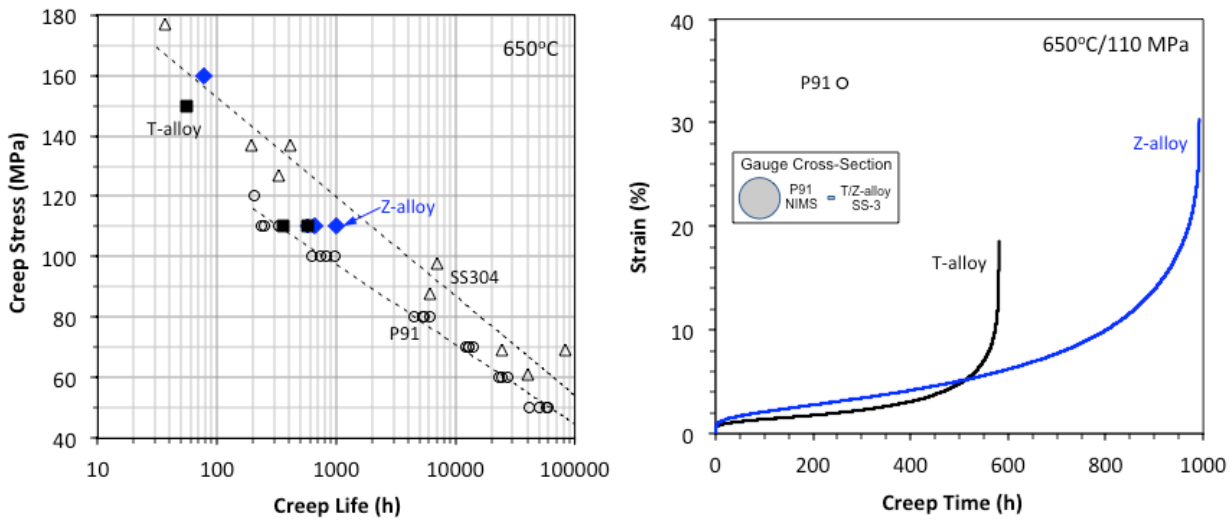

Figure 15. Plots of stress-creep life and strain-creep time showing the creep resistance of T- and Z-alloys at 650°C.

4.4 THERMAL AGING EFFECTS ON MECHANICAL PROPERTIES

Thermal aging is expected to exert significant effects on microstructures such as dislocation density, new precipitates formation and the stability of pre-existing precipitates, resulting in potential changes in mechanical properties. For example, the thermal aging experiment on alloy LNTZ at 700°C for 7800 h led to the formation of many fine particles as shown in the BEIs of Figure 8. The hardness of the aged sample was measured to be 176 ± 4 HV1 that is comparable to the as-received condition of 179 ± 9 HV1. Type SS-3 specimens of the developed T- and Z-alloys are being aged at 600 and 700°C, targeting up to 5000 h by late this year. The aging effect on hardness, tensile properties and creep resistance will be evaluated.

5. ION-IRRADIATION EXPERIMENTS

A total of twelve T-, Z-, and L-alloys were irradiated using 2 MeV protons at 420°C up to either ~0.1 dpa or ~1 dpa. Vickers microhardness measurements were performed on all irradiated samples and their unirradiated counterparts. Precipitate formation during irradiation was investigated by X-ray diffraction (XRD). Investigations for identifying radiation-induced microstructural evolution including morphologies and chemistry have been initiated. The following sections describe the irradiation experiments and experimental findings.

5.1 EXPERIMENTAL PROCEDURE

5.1.1 Proton Irradiation

Prior to ion irradiation, all alloys were cut into 5×5 mm^2 pieces and polished to mirror finish thin foils, from which 3 mm diameter TEM discs were punched out and cleaned ultrasonically as shown in Figure 16.

Figure 16. Photos of as-received alloy samples (left) and prepared polished 3-mm disks (right).

A total of twelve T-, Z-, and L-alloys have been irradiated by 2 MeV protons using the 1.7 MV ion beam accelerator at the University of Wisconsin-Madison. The 3 mm diameter samples were attached to a stainless steel sample holder using water-soluble carbon paste. The incident ion beam, normal to the sample face, was rastered across a well-defined aperture exposing the samples uniformly to the H ions. The beam current ranged between 10-13 μA, resulting in a proton flux of about 3×10^{13} p/(cm^2s) and a dpa rate of 3×10^{-6} dpa/s. The sample temperature of 420°C was maintained through a combination of beam heating and air cooling on the back side of the samples, recorded on the right and left sides of the sample holder using two type-K thermocouples (see Figure 17). The irradiation chamber pressure was at or below 1×10^{-6} Torr before and during the irradiation. The irradiation with 2.0 MeV protons, corresponding to a projected range R_p = 19 μm (see Figure 18), was conducted on the samples to fluences of 1.1×10^{18} and 1.1×10^{19} p/cm^2, which correspond to damage levels of ~0.1 and ~1 dpa at a depth of 15 μm, respectively.

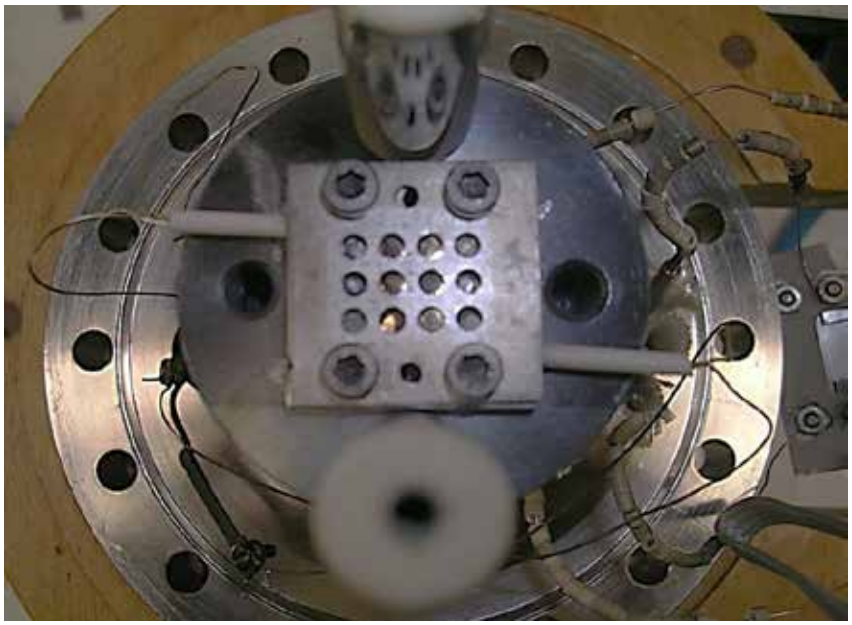

Figure 17. Sample and thermocouple arrangement in the irradiation stage with six samples ready for 2 MeV proton irradiation at 420°C up to ~1 dpa.

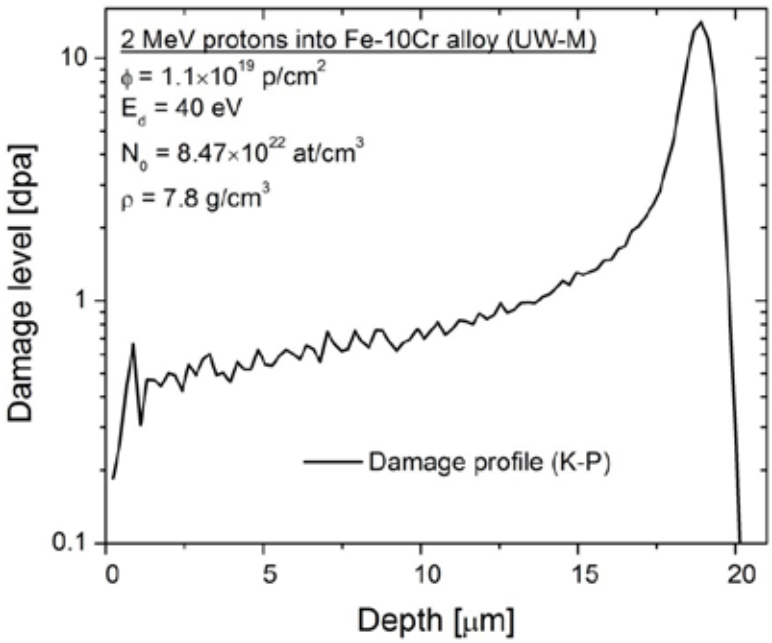

Figure 18. Damage profile in a model Fe-15Cr alloy irradiated by 2 MeV protons to a level of 1 dpa at 15 µm. Calculation was performed using SRIM-2012.03 assuming th displacement threshold energies to be 40 eV for all elements.

5.1.2 X-Ray Diffraction and Transmission Electron Microscopy

Structural characterization was performed using X-ray diffraction (XRD) as well as TEM in both conventional and scanning modes coupled with energy dispersive X-ray spectroscopy (STEM/EDS) to understand the evolution or suppression of any phases during irradiation in the developed alloys.

The XRD analysis of all the alloys was performed on Bruker D8 Discovery at 50 kW and 1000 μA, using Cu anode with λ=1.54184 Å. A 0.5 mm incident slit and 0.5 mm collimator in combination with the Montel mirror and Soller mount were used. The 2D Vantec 500 detector was located 200 mm from the sample. Standard θ-2θ scans were taken at the range between 20°-85° with three steps (300 s/step) starting at 2θ = 25° and increment of 25°. In order to include the maximum number of grains (as large as a couple of hundreds of micrometers for L-alloys) in the XRD analysis, the x-y rastering (1 mm by 1 mm, x-speed: 0.1 mm/s, y-speed: 0.2 mm/s) with simultaneous phi rotation (360°, speed 72°/s) was performed. Same parameters were used for all investigated samples and 1-3 samples per condition, i.e., 0 (reference), 0.1, and 1 dpa, for all the alloys were measured.

X-ray penetration depth was calculated to determine the thickness of the damage zone being investigated. The mass absorption coefficients for Fe and Cr for the Cu-Kα radiation are 302 and 247 cm^2/g. Using the L-alloys with a nominal density of 7.77 g/cm^3 as an example, the mass absorption coefficient of this series of alloys is expressed as follows:

$$\left(\frac{\mu}{\rho}\right)_{L-alloys} = 0.85\times302 + 0.15\times247 = 294\ (\mathrm{cm}^2/\mathrm{g})$$

The linear absorption coefficient is then:

$$\mu_{L-alloys} = 294\times7.77 = 2284\ (\mathrm{cm}^{-1})$$

Therefore the half value layer thickness is:

$$x = \frac{0.693}{2284} = 3\ \mu m$$

which is much shorter than the implantation depth (about 20 μm).

TEM samples were prepared in a Zeiss 1500XB focused ion beam (FIB) system. Platinum coating was deposited to protect specimen surface before cutting. TEM lamellae were created by coarse trenching to produce samples of 20 μm × 15 μm × 1 μm in dimensions using the FIB technique. The samples were then welded to a copper TEM grid for final thinning to a final thickness of roughly 100-200 nm using 30 kV gallium ions and further polished using 5 kV gallium ions. The TEM lamellae were finally cleaned with a Fischione's Model 1040 Nanomill with 900 eV Ar ions for 30 min at each side. A Titan STEM with CEOS (corrected electron optical systems) probe aberration corrector operated at 200 kV, equipped with a high-angle angular-dark-field (HAADF) detector and an EDS system, was used for microstructure and composition analysis. The probe size for EDS line-scan was less than 1 nm with a step size of ~1 nm.

5.1.3 Vickers Microhardness

Low load Vickers microhardness tests were performed at a load of 25 gf with two indents per sample. Indentation depth varied between 1.9 – 2.6 μm depending on the sample type and dpa level, which may still incorporate substrate effects. In the future, nano-indentation will be performed to obtain data which comply more specific to the irradiated zone.

5.2 RESULTS

5.2.1 L-Alloys

All L-alloys showed some discoloration (see Figure 19) after the proton irradiation. Further TEM analysis suggests a build-up layer of ~1 μm thick titanium oxide on the surface (see Figure 23).

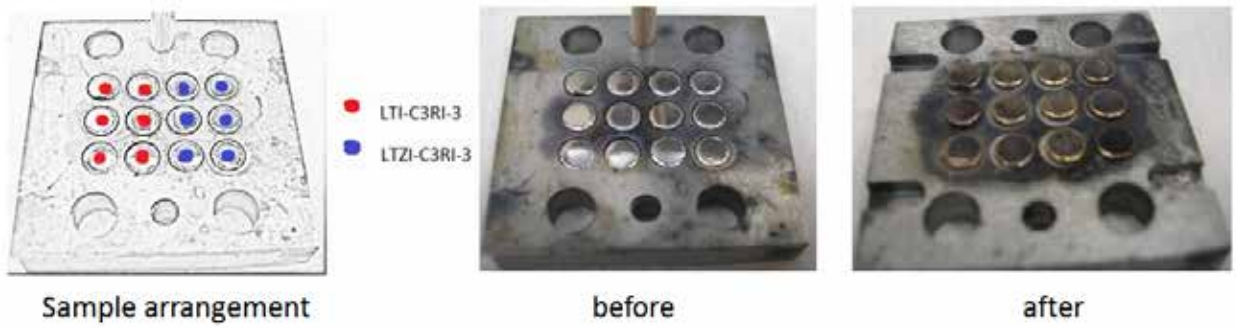

Figure 19. L-alloy sample arrangement and appearance before and after 2 MeV proton irradiation at 420°C up to 0.1 dpa.

The XRD data of L-alloy LTZ1 as shown in Figure 20 indicate the evolution of certain new phases as a result of irradiation, particularly at 1 dpa damage levels. These are speculated to be Ti-rich phases however their exact stoichiometry has yet to be confirmed. To more accurately confirm these phases as well as their morphology and spatial distribution, TEM samples are presently being prepared using FIB technique to minimize any aberrations due to the magnetic nature of the samples. The as-received LTZ1 was denuded of precipitates at grain boundaries (GBs) and a high density of dislocation was found in the samples (Figure 21). After irradiation at a damage level of 0.1 dpa, Ti and W rich phases were found at GBs (Figure 22). As the damage level reached 1 dpa, a thick Ti-rich phase was observed at the sample surface (Figure 23). It was possibly induced by the oxidation of partial outward diffusing Ti. Similar Ti-rich phase can also be found in the LT1 sample (Figure 24). However, the damage in the irradiated samples has not been well characterized. The FIB samples were still too thick with high surface damages. Further ion polishing at lower energies could help reveal the fine microstructure in the irradiated samples. Additionally, α'-phase (Cr-rich) would form during the proton irradiation due to the high Cr content in the L-alloys as suggested in Figure 3, which is thermodynamically stable at temperatures below ~500°C. Neutron irradiation studies on ferritic steels at 380-550°C have observed the presence of α'-phase in alloys having Cr greater than 10 wt.% [17]. Based on the limited TEM data, no firm scientific conclusion could be made to summarize the irradiation effects in these samples, but this work is ongoing.

Radiation hardening at 420°C was clearly observed in all the alloys as shown in Figure 25. L-alloys performed worst with ~120% of increase in hardness at 1 dpa. T-alloys exhibited the least radiation hardening after up to ~2 dpa irradiation. Z-alloys showed a large variation in hardening from ~30% comparable to the T-alloys to ~90%, indicating that the alloy composition (or phase components as shown in Figure 2 and Figure 6) can significantly adjust the radiation hardening of this series of alloys. According to Gupta's work on 2 MeV proton-irradiated T91 [18], significant recovery in radiation hardening occurred at irradiation temperatures above 450°C. The irradiation temperature at 420°C in this work still reflects dominant radiation hardening effects to the T-alloys and expect to be applicable to the Z- and L-alloys.

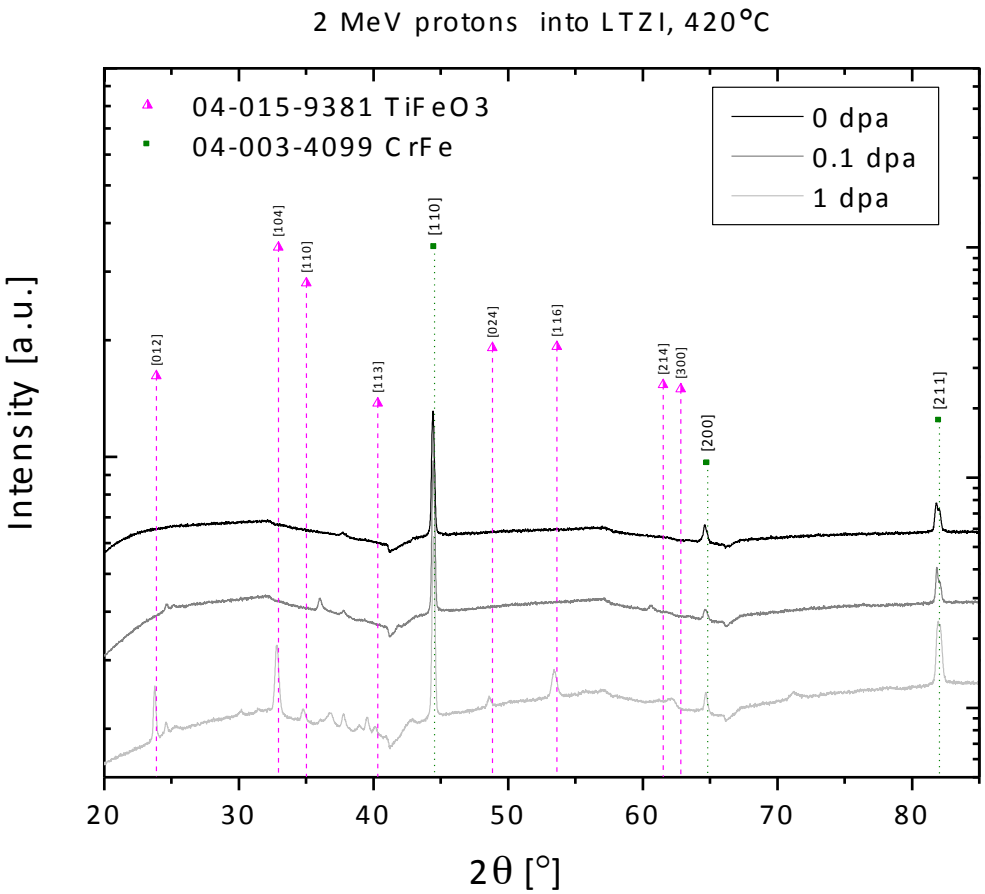

Figure 20. XRD patterns of L-alloy LTZ1 at various damage levels. The possible Ti-rich peaks are marked in magenta.

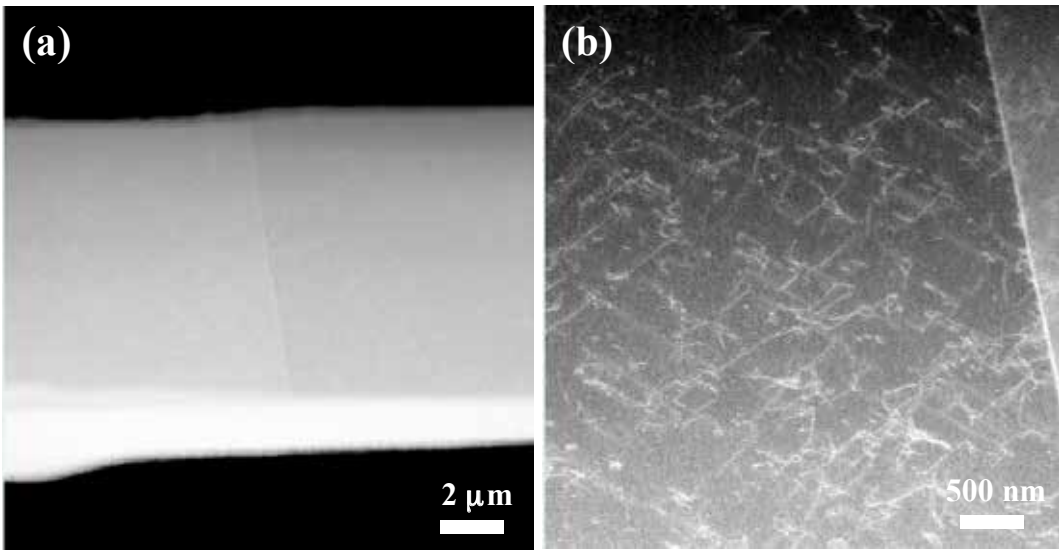

Figure 21. STEM image of L-alloy LTZ1 before proton irradiation: (a) low magnification and (b) high magnification.

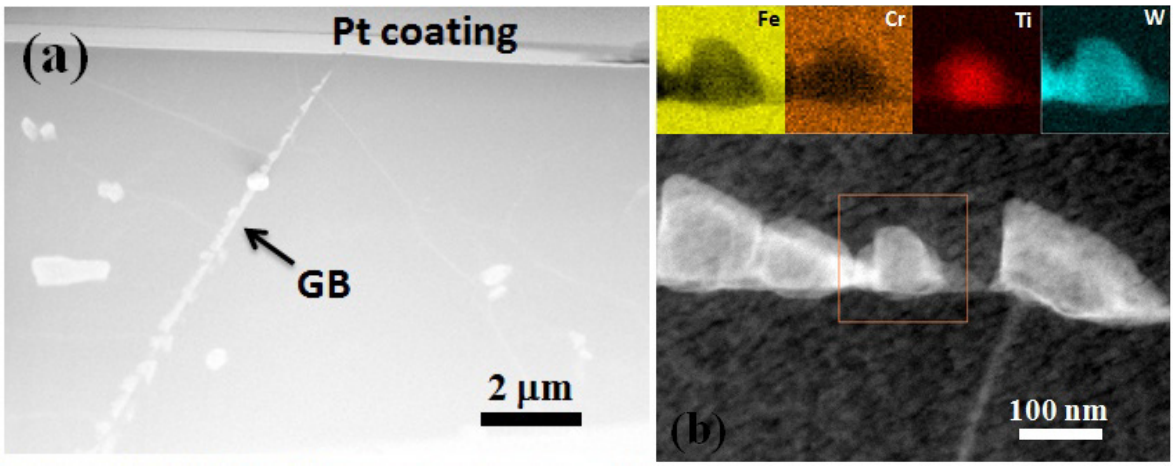

Figure 22. (a) STEM image and (b) EDS mapping of L-alloy LTZ1 irradiated with protons at 420°C for up to 0.1 dpa.

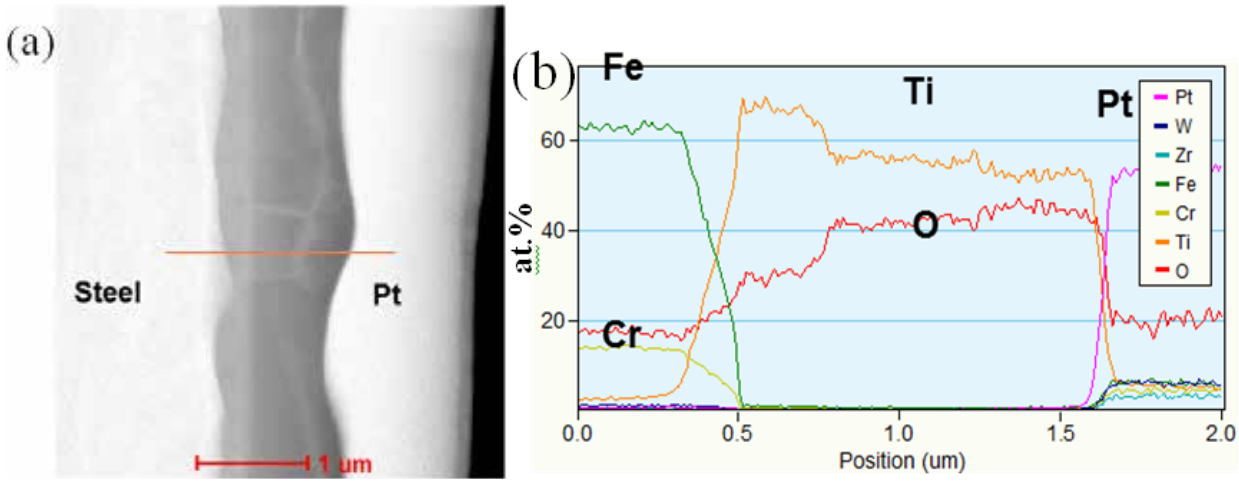

Figure 23. (a) STEM image and (b) EDS line-scan of L-alloy LTZ1 irradiated with protons at 420°C for up to 1 dpa.

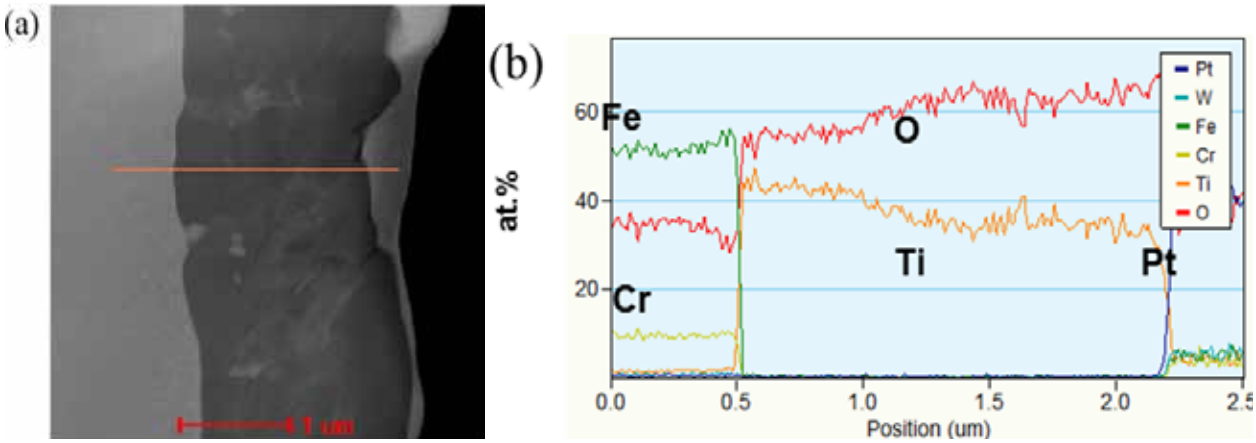

Figure 24. (a) STEM image and (b) EDS line-scan of L-alloy LT1 irradiated with protons at 420°C for up to 1 dpa.

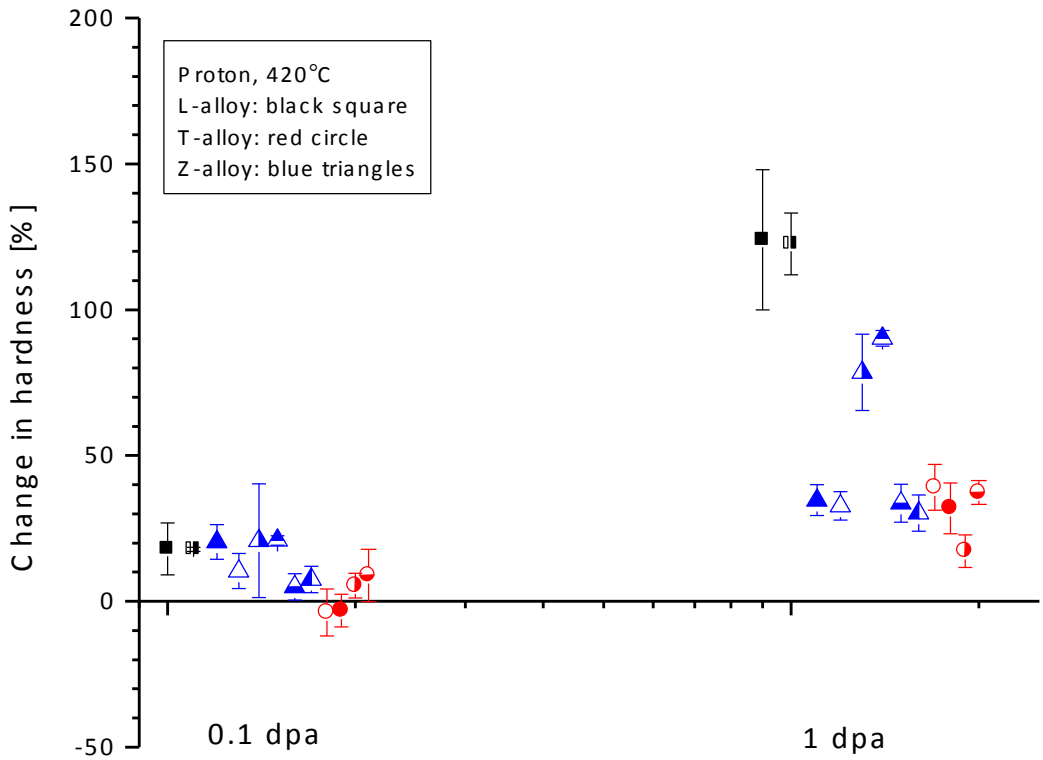

Figure 25. Vickers hardness (25 gf) changes of the irradiated advanced alloys as compared to their non-irradiated condition.

5.2.2 T- and Z-Alloys

Post-irradiation discoloration was not observed on the surfaces of the T- and Z-alloys. All the T-alloys seem to be resistant to precipitate formation or phase changes due to proton irradiation (see Figure 26 and Figure 27). Almost no change in XRD spectra is observed between various damage levels, which also results in the least hardness changes (see Figure 25) with only up to 10% of hardening at 0.1 dpa and less than 40% at 1 dpa. Ti_xO_y layer build-up was not observed in those alloys despite the fact that they had similar Ti content to L-alloys.

Z-alloys underwent some phase change during proton irradiation at various damage levels (see Figure 28), however not as drastic as the L-alloys. Fe_2Zr hexagonal phase could be clearly identified, especially in the samples with a higher Zr content (see Figure 29). In almost all the Z-alloys and some of the T-alloys, a new peak at 2θ ~26° showed up after proton irradiation, which was impossible to identify. In terms of hardness, the Z-alloys appear to harden a little bit more at a certain damage level than the T-alloys, however this trend has to be confirmed for Fe-ion irradiated samples where high dpa levels can be achieved.
αααα

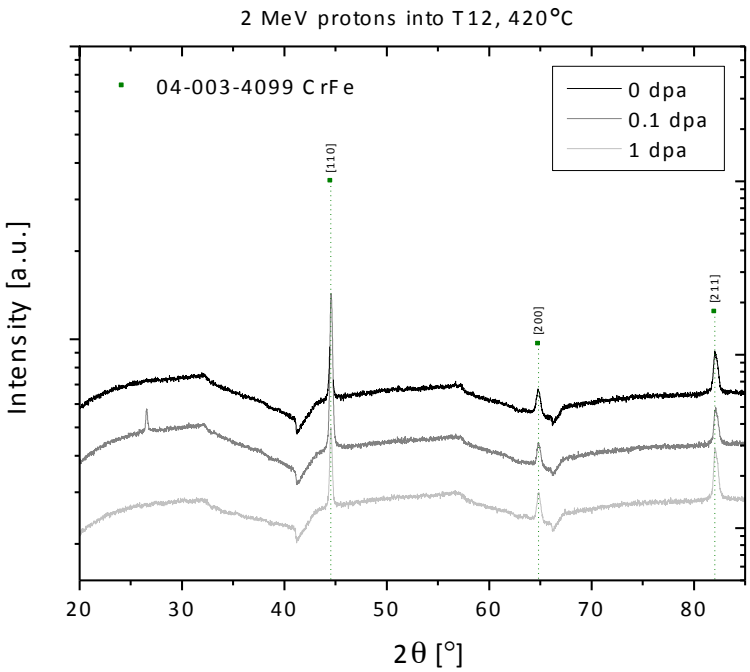

Figure 26. XRD patterns of T-alloy T12 at various damages levels.

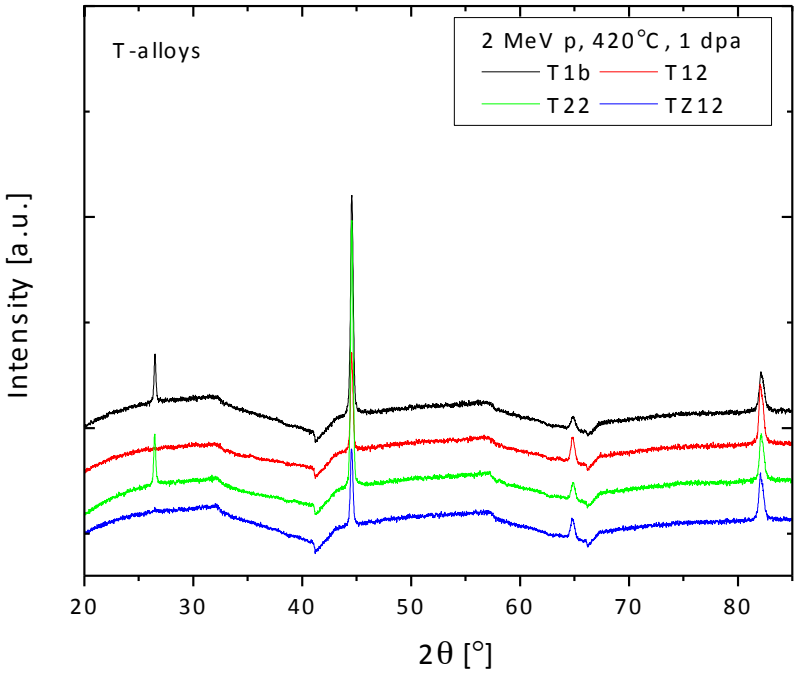

Figure 27. XRD patterns of T-alloys irradiated up to 1 dpa. Main peaks at 2θ of 45°, 65°, and 82° correspond to diffraction from CrFe (PDF04-033-4099).

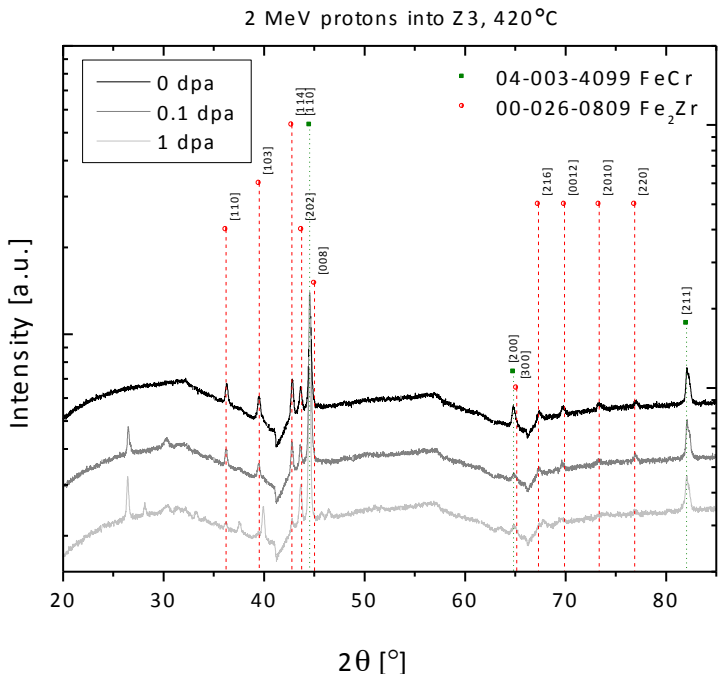

Figure 28. XRD patterns of Z-alloy Z3 at various damages levels. The possible Zr-rich peaks are marked in red.

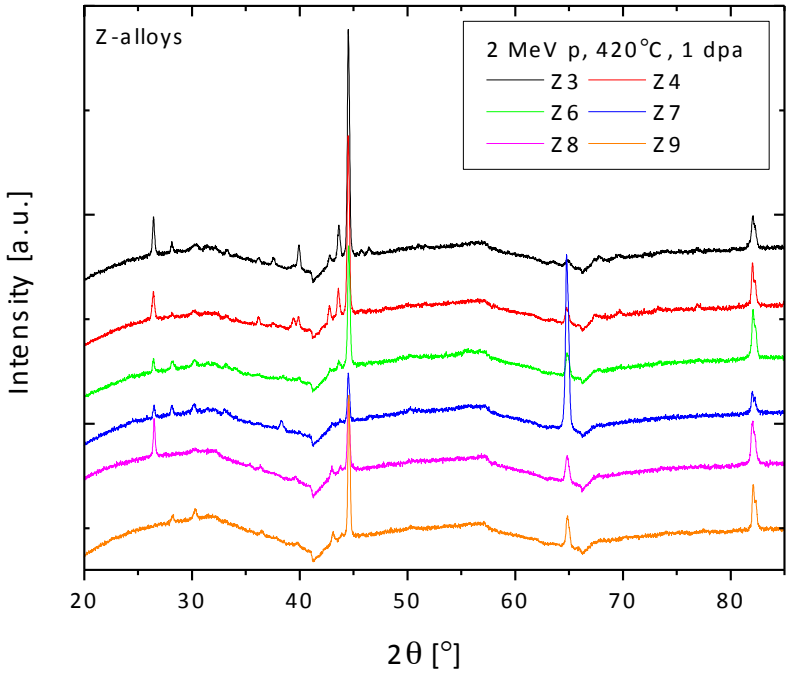

Figure 29. XRD patterns of Z-alloy irradiated up to 1 dpa. Main peaks at 2θ of 45°, 65°, and 82° correspond to diffraction from CrFe (PDF04-033-4099).

6. SUMMARY

Using the thermodynamic database that was developed in this project, three series of ferritic alloys have been developed due to the inherent void swelling resistance of ferrite (bcc) as compared to austenite (fcc). They are T-alloys (9Cr FM steels), Z-alloys (intermetallic-strengthened Fe-Cr-Zr alloys), and L-alloys (15Cr ferritic steels). Unlike 9Cr FM steels such as T-alloys and P91, Z- and L-alloys are full ferritic alloys, without the ferrite-austenite phase transformation during heating and cooling, leading to easier alloy fabrication. The experimental lab heats (~0.45 kg each) were produced by vacuum arc melting and drop casting followed by different thermomechanical processing for respective alloy series. Chemical analysis indicated that oxygen impurity could not be consistently well controlled in the small lab heats. A larger heat (~12.7 kg) was produced by Carpenter Technology Corporation and achieved a low level of oxygen content, suggesting oxygen impurity can be well controlled in larger scale castings at industrial facilities.

As compared to P91, T-alloys were designed to have increased MX, reduced $M_{23}C_6$, and eliminated Z-phase for better high temperature strength. Significantly finer MX (~5 nm) precipitates with about two orders of magnitude increase in density have been observed in some of the T-alloys. Z-alloys were designed to have fine eutectic structure of ferrite and Fe_2Zr Laves phase. The fraction of the eutectic component has resulted in significant difference in microstructures of the Z-alloys. Additionally, thermal aging favors the formation of a large number of fine Laves phase particles on the order of ~100 nm in the ferritic matrix. L-alloys were designed to have strengthening sources primarily from Fe_2W-type Laves phase, assisted with grain refinement by Zr addition. Thermal aging of a L-alloy at 700°C for 7800 h manifested the formation of a large number of such Laves particles in a size ranging from as small as ~90 nm in the ferritic matrix up to a few hundred nanometers at grain boundaries. The formation of such Laves particles did not result in significant changes in hardness. Thermal aging of the T- and Z-alloys at 600 and 700°C, targeting up to 5000 h, is in progress. The aging effect on microstructures and mechanical properties will be explored.

Vickers hardness measurements indicate that T-alloys have hardness close to the upper bound of P91 (265 HV) but L-alloys are slightly lower than the lower bound of P91 (196 HV). Z-alloys exhibited a large variation in hardness from the lower bound of P91 to the values significantly higher than the upper bound of P91. Due to the limited size of the developmental lab heats, type SS-3 miniature specimens were used for tensile and creep rupture tests. L-alloys showed the lowest strength that is lower than or comparable to P91. T-alloys exhibited the highest strength, significantly higher than P91 at the testing temperatures up to 800°C. Depending on specific alloys, Z-alloys displayed strength either inferior or superior to P91 at temperatures less than ~500°C. However, the high temperature (above 500-600°C) strength of the Z-alloys became similar, which is comparable to T-alloys and noticeably greater than P91. The total elongation of the three series of alloys was lower or comparable to P91, most of which are satisfactory considering the significantly smaller testing specimens used in this work as compared to the regular specimens of P91, e.g., 1.16 mm^2 of SS-3 in this work vs. 78.5 mm^2 of P91 for gauge cross-section. Creep testing of T- and Z-alloys at 600 and 650°C indicated that Z-alloys had creep resistance comparable or superior to T-alloys, both of which have improved creep resistance as compared to P91.

A total of twelve T-, Z-, and L-alloys were irradiated using 2 MeV protons at 420°C up to either ~0.1 dpa or ~1 dpa. Vickers microhardness measurements indicated the largest radiation hardening of the L-alloys (~120%) and the smallest hardening of the T-alloys (~15-40%) after ~1 dpa irradiation. The Z-alloys exhibited a large variation in hardening (~30-90%), suggesting a strong microstructure effect. XRD and STEM/EDS investigations suggested the formation of a large amount of radiation-induced precipitates in the L-alloys and a small amount in the Z-alloys, but none in the T-alloys, which is

qualitatively consistent with the largest hardening of the L-alloys and the smallest hardening of the T-alloys. Detailed microstructural characterization of the irradiated samples is in progress.

According to the collected results, the L-alloys exhibited low strength, high radiation hardening, and dynamic precipitation of secondary precipitates during thermal aging and irradiation. Additionally, as suggested by the thermodynamic calculations, α'-phase (Cr-rich) is expected to precipitate during long-term aging and accelerated by irradiation at temperature below ~500°C due to the high Cr content in the L-alloys. Therefore, alloy development of L-alloys will not be continued. Future alloy development efforts will be focused on the T- and Z-alloys, which have superior high temperature strength and radiation resistance.

REFERENCES

[1] N. Baluc, On the potentiality of using ferritic/martensitic steels as structural materials for fusion reactors, FT/1-1Rb

[2] H. Mimura, M. Ohgami, H. Naoi, T. Fujita, Properties of 9Cr-1.8W steel with high creep strength for USC boiler piping and tubing applications, in: D. Coutsouradis (Eds.), Materials for Advanced Power Engineering, Kluwer Academic Publishers, The Netherlands, 1994, pp. 361.

[3] B. Raj, M. Vijayalakshmi, Ferritic steels and advanced ferritic-martensitic steels, in: R.J.M. Konings, T.R. Allen, R.E. Stoller, S. Yamanaka, Comprehensive Nuclear Materials, Elsevier, 2012.

[4] K. Maruyama, K. Sawada, J. Koike, Strengthening mechanisms of creep resistant tempered martensitic steel, ISIJ International 41 (2001) 641-653.

[5] L. Tan, T.S. Byun, Y. Katoh, L.L. Snead, Stability of MX-type strengthening nanoprecipitates in ferritic steels under thermal, stress and ion irradiation, Acta Materialia 71 (2014) 11-19.

[6] D.G. Morris, M.A. Munoz-Morris, L.M. Requejo, Acta Materialia 54 (2006) 2335-2341.

[7] N. Shigenaka, S. Ono, Y. Isobe, T. Hashimoto, H. Fujimori, S. Uchida, Effect of zirconium addition to austenitic stainless steels on suppression of radiation induced chromium segregation at grain boundaries under ion irradiation, Journal of Nuclear Science and Technology 33 (1996) 577-581.

[8] M.J. Hackett, J.T. Busby, M.K. Miller, G.S. Was, Effects of oversized solutes on radiation-induced segregation in austenitic stainless steels, Journal of Nuclear Materials 389 (2009) 265-278.

[9] L. Kaufman, B. Uhrenius, D. Birnie, K. Taylor, Coupled pair potential, thermochemical and phase-diagram data for transition-metal binary-systems .7., CALPHAD 8 (1984) 25-66.

[10] N. Saunders and A.P. Miodownik, CALPHAD (Calculation of Phase Diagrams): A Comprehensive Guide (1st Ed.), Elsevier, New York, 1998.

[11] Muggianu, Yves M., Michele Gambino, and Jean P. Bros, Enthalpies of formation of liquid alloys bismuth-gallium-tin at 723.deg.K. Choice of an analytical representation of integral and partial excess functions of mixing, Journal de Chimie Physique et de Physico-Chimie Biologique 72 (1975) 83-91.

[12] http://www.computherm.com

[13] L. Tan, Y. Yang, Progress report on the mechanical testing and thermal aging of Zr-bearing ferritic steels, ORNL/TM-2013/360, September 2013.

[14] NIMS Creep Data Sheet No. 43A, National Institute for Materials Science, Japan, 2014.

[15] Y. Yang, L. Tan, H. Bei, J.T. Busby, Thermodynamic modeling and experimental study of the Fe-Cr-Zr system, Journal of Nuclear Materials 441 (2013) 190-202.

[16] NIMS Creep Data Sheet No. 32A, National Institute for Materials Science, Japan, 1995.

[17] P.J. Maziasz, Formation and stability of radiation-induced phases in neutron-irradiated austenitic and ferritic steels, Journal of Nuclear Materials 169 (1989) 95-115.

[18] G. Gupta, Z. Jiao, A.N. Ham, J.T. Busby, G.S. Was, Microstructural evolution of proton irradiated T91, Journal of Nuclear Materials 351 (2006) 162-173.